Reproductive Biology 25 (2025) 101040

Contents lists available at ScienceDirect

Reproductive Biology

journal homepage: www.journals.elsevier.com/reproductive-biology

Original Article

Vitamin D_3 and insulin treatment affects porcine follicular fluid-derived extracellular vesicles characteristics and proteome cargo

Kinga Kamińska [a,b], Bianka Świderska [c], Agata Malinowska [c], Jakub Barbasz [d], Małgorzata Grzesiak [a,*]

[a] Department of Endocrinology, Institute of Zoology and Biomedical Research, Faculty of Biology, Jagiellonian University, Gronostajowa 9, Krakow 30-387, Poland
[b] Doctoral School of Exact and Natural Sciences, Jagiellonian University, Krakow, Poland
[c] Mass Spectrometry Laboratory, Institute of Biochemistry and Biophysics, Polish Academy of Sciences, Pawinskiego 5a, Warszawa 02-106, Poland
[d] Jerzy Haber Institute of Catalysis and Surface Chemistry, Polish Academy of Sciences, Niezapominajek 8, Krakow 30-239, Poland

ARTICLE INFO

Keywords:
Extracellular vesicles
Vitamin D_3
Insulin
Follicular fluid
Pig

ABSTRACT

The study aimed to investigate whether vitamin D_3 and insulin alone or in co-treatment can influence characteristics and protein cargo of the porcine follicular fluid (FF)-derived extracellular vesicles (EVs). To this end, medium antral follicles were cultured *in vitro* alone (C; control) or with 1α,25$(OH)_2D_3$ (VD; 100 ng/mL) and insulin (I; 10 ng/mL) separately or in combination (VD+I). The properties of the FF-EVs were assessed by transmission electron microscopy, nanoparticle tracking analysis, electroforetic light scattering, and flow cytometry, while the global proteomic analysis was conducted by liquid chromatography-tandem mass spectrometry coupled with the TMT-isobaric mass tag labeling. In all groups, particles represented a typical cup-shaped morphology, ranged between 50 and 450 nm in diameter, and expressed marker proteins, such as CD63 and CD81. The I treatment decreased the concentration and average size of the FF-EVs, while VD reversed only the effect on the particle concentration. Proteomic analysis revealed 48 differentially abundant proteins (DAPs) between examined groups, whilst greater amount of DAPs was identified following VD and I treatment alone than in co-treatment. Functional analysis showed that VD alone or in combination with I decreased predominantly the abundance of ribosomal proteins. In the I group, proteins involved in oxidative stress were down-regulated. We also found that the FF-EVs are carriers of adiponectin, which was up-regulated in the VD+I group. To sum up, VD and I seem to be novel modulators of the porcine FF-EVs characteristics and protein cargo, and thereby could modify ovarian follicle function *via* the EV-mediated pathway.

1. Introduction

The ovary is a unique, permanently remodeling endocrine gland. The ovarian functions, namely the production of the oocytes and the secretion of steroid hormones, are supported by the ovarian follicles to ensure successful reproduction in females [1]. Follicle development is deployed in the framework of the endocrine regulation within hypothalamic-pituitary-ovarian axis [2]. Apart from that also intra-follicular autocrine and paracrine communication, including hormones and growth factors released by the oocyte and somatic cells (granulosa and theca cells), is vital for the follicular steady growth and function [3]. In recent years, a novel pathway of the cross-talk between the oocyte and follicular cells *via* extracellular vesicles (EVs) was extensively described [4].

EVs represent a heterogeneous population of lipid-bilayer membrane-enclosed vesicles that are secreted across various cell types [5] and transport their attendant cargo, including proteins, lipids, and nucleic acids (miRNA, mRNA, and DNA) [6]. The existence of EVs released by the ovarian follicle cells has been unveiled in human [7], equine [8], bovine [9] and porcine [10] follicular fluid (FF), suggesting their pivotal role in the cross-talk between the oocyte and surrounding somatic cells. So far, research on different mammalian species revealed the impact of the FF-EVs on cumulus cells, influencing thereby the oocyte competence and maturation [for review see 11]. It was also found that the FF-EVs cargo, predominantly miRNA, activates plethora of ovarian signaling pathways involved in granulosa cell proliferation, inflammatory response, steroids production and follicular development (for review see 12]. The FF-EVs concentration and molecular

* Corresponding author.
E-mail address: m.e.grzesiak@uj.edu.pl (M. Grzesiak).

https://doi.org/10.1016/j.repbio.2025.101040
Received 3 March 2025; Received in revised form 1 May 2025; Accepted 27 May 2025
Available online 3 June 2025

composition depend on the follicle size [9,10], hormonal and metabolic status [8,13], and oxidative stress [14]. Furthermore, the FF-EVs can contain highly diverse biomolecules upon ovarian pathologies such as polycystic ovarian syndrome (PCOS), indicating their diagnostic potential [15,16]. Therefore, the examination of specific factors that can modify the characteristics and cargo of the FF-EVs could provide a novel mechanistic insight into normal follicle development and its pathologies.

Vitamin D_3 (VD) has been recognized as a regulator of ovarian functions in humans [17] and animal species [18]. Multiple evidence suggests that VD influences follicle formation, development and maturation, steroids biosynthesis, as well as exerts anti-oxidant or anti-apoptotic effects [17]. Furthermore, VD is proposed as an alternative therapy in PCOS treatment, especially to ameliorate metabolic symptoms, such as insulin resistance and hyperinsulinemia, observed in the ovary as well [19]. Given that insulin (I) gene promoter possesses VD response element there is a direct link between VD and I action [20].

Recently we have shown that VD and/or I *in vitro* treatment altered proteome composition of granulosa and theca interna cells within porcine ovarian follicle, modulating thereby cell proliferation, cell cycle progression, and cholesterol transport, which are important for proper ovarian functioning [21]. Taken together above findings, the involvement of EVs in the intrafollicular communication [12], as well as the crucial role of VD in the ovary under physiological and pathological conditions [22], we hypothesize that VD and I alone or in combination influence characteristics and proteome cargo of the porcine FF-EVs that can pave a new pathway for understanding of ovarian processes regulation. To this end, the FF-EVs concentration and size distribution were determined by nanoparticle tracking analysis (NTA), zeta potential was measured using electroforetic light scattering (ELS), the morphology of particles was assessed by transmission electron microscopy (TEM), and their phenotypical analysis was performed using flow cytometry (FC). In addition, the global analysis of the FF-EVs proteome cargo was conducted employing tandem mass tag (TMT)-labeled liquid chromatography-tandem mass spectrometry (LC-MS/MS) to reveal an in-depth molecular mechanism underlying VD and I cross-talk within the ovarian follicle using pig as a model.

2. Materials and methods

2.1. Animals and tissue collection

The animal study was conducted in accordance with the regulations outlined in the Act of January 15, 2015 concerning the Protection of Animals Used for Scientific or Educational Purposes and Directive 2010/63/EU of the European Parliament and the Council of September 22, 2010 regarding the protection of animals used for scientific purposes.

Porcine ovaries were harvested *post mortem* from sexually mature crossbred gilts (Large White × Polish Landrace) of similar age (6–8 months) and weight (120 ± 130 kg) at a local abattoir under veterinarian control. The ovaries were immediately transported to the laboratory in ice-cold phosphate-buffered saline (PBS; pH 7.4) supplemented with antibiotic-antimycotic solution (AAS 100 ×, Sigma-Aldrich, St. Louis, MO, USA) within ~1 h. Healthy, medium antral follicles (3.0–6.9 mm in diameter) from ovaries at the follicular phase of the estrous cycle were dissected using scissors for further *in vitro* culture. The phase of the estrous cycle was verified based on ovarian morphology and corpus luteum quality according to Akins and Morrissette [23].

2.2. Ovarian follicle in vitro culture and FF collection

Ovarian follicle *in vitro* culture was performed as previously described [21,24]. Briefly, whole porcine ovarian follicles (12 follicles from different animals/group per one biological repetition; $n = 4$; a total number of follicles used was 192) were pre-incubated for 3 h on a Falcon Organ Culture Dish (Fisher Scientific, Schwerte, Germany) equipped with a triangular stainless steel grid in M199 medium (Sigma-Aldrich, St. Louis, MO, USA) supplemented with 1 % exosome-depleted fetal bovine serum (FBS) (Thermo Fisher Scientific, Wilmington, DE, USA) and AAS. Then the medium was replaced by fresh M199 medium containing 0.1 % exosome-depleted FBS and AAS, and further incubation was carried out for 12 h with medium alone (control, C group) or with addition of $1\alpha,25(OH)_2D_3$ (100 ng/mL; VD group), I (10 ng/mL; I group) or both $1\alpha,25(OH)_2D_3$ and I (VD+I group). VD and I were dissolved in ethanol and the final concentration of the solvent in culture medium was below 0.1 %. Doses of VD and I were chosen based on the literature data and our previous studies [25–27]. All cultures were maintained at standard conditions (37°C, 5 % CO_2/95 % O_2) and the experiment was performed in four independent repetitions (Fig. 1).

After *in vitro* culture, ovarian follicles were rinsed with PBS, FF was aspirated using a syringe and pooled from 12 follicles within group into one sample. Next, FF samples were subjected to serial centrifugation at 300 ×*g*, 2000 ×*g* and 5000 ×*g* at 4℃ for 10 min each to remove remnant cells, cell debris and apoptotic bodies, respectively. Finally, the FF samples were concentrated to 500 μL using Amicon® Ultra-2ml centrifugal filter (10 kDa cut-off; Merck Millipore, Burlington, MA, USA).

2.3. Size-exclusion chromatography

EVs from all FF samples were isolated using SEC according to previously described protocol [28,29]. Briefly, 500 μL of FF samples were applied on top of the filter in a benchtop SEC columns (Econo-pac® Disposable chromatography column; Bio-Rad Laboratories Inc., Berkeley, CA, USA) filled with SEC resin (Sepharose 4 fast flow™; Cytiva, Uppsala, Sweden), using PBS as the eluent. The EV-enriched fractions 5–9 (2.5 mL) were collected and concentrated using Amicon® Ultra-2ml centrifugal filter (10 kDa cut-off) by centrifuging at 3000 ×g at 4℃ until obtaining a final volume of 500 μL for EVs characteristic or 100 μL for proteomic analysis. The fractions 5–9 were previously assessed as those with the greatest concentration of EVs and the lowest content of contaminating proteins [29]. The FF-EV samples were stored at −80℃ for further analysis.

2.4. Transmission electron microscopy

The presence and morphological characteristic of the FF-EVs was performed using TEM. Each FF-EV sample was deposited on carbon-coated formvar 300 mesh grids for 20 min to adsorb. Afterward, the samples were washed with distilled water and contrasted with 2 % uranyl acetate (Chemapol, Prague, Czech Republic). Finally, the grids were air dry and observed under the JEOL JEM 2100HT transmission electron microscope (JEOL, Tokyo, Japan) at accelerating voltage 80 kV. Images were taken by using 4k× 4k camera (TVIPS) equipped with EMMENU software ver. 4.0.9.87.

2.5. Nanoparticle tracking analysis

The concentration and size distribution of the FF-EVs were determined by NTA using LM10 Nanosight instrument (Malvern Instruments Ltd., Malvern, UK) equipped with a sCMOS camera (Hamamatsu Photonics, Hamamatsu, Japan) and a 405 nm blue laser. Before analysis, each EV-enriched sample was diluted 1:1000 with Dulbecco's PBS (DPBS) without Ca^{2+} and Mg^{2+} (Sigma-Aldrich) to ensure optimal particle concentration. Data were analyzed using NTA analytical software (version 3.1 Build 3.1.45). Five 30 seconds video clips per sample at 25 frames per second were obtained and used to measure particles concentration and size. The analysis was conducted under the following settings: camera level at 14, shutter value of 1259 and slider gain of 366.

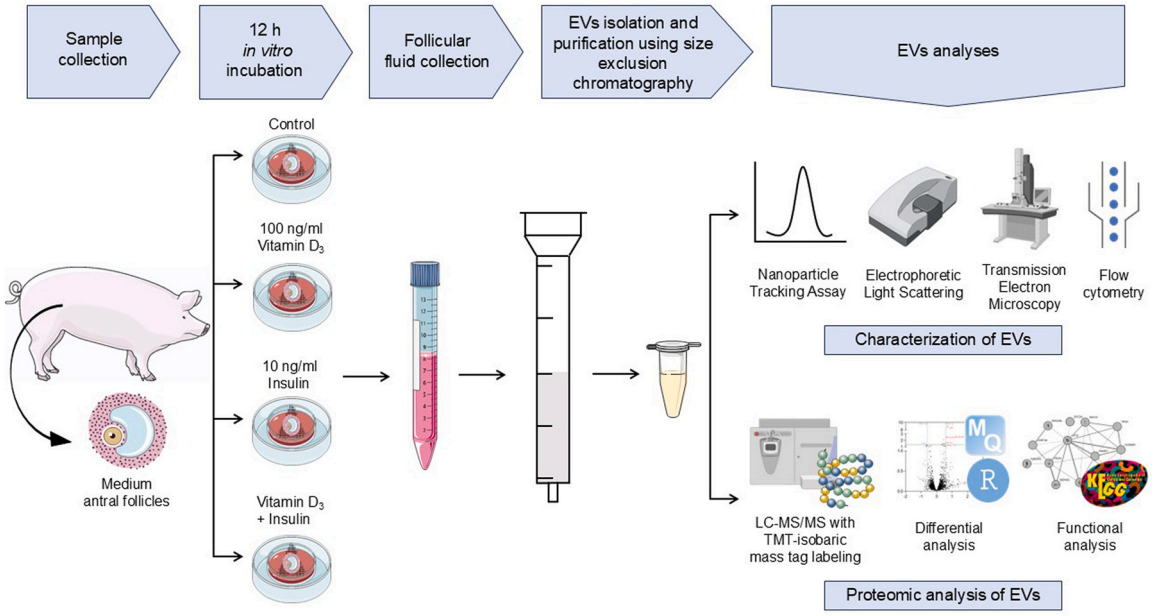

Fig. 1. Schematic diagram showing experimental design, stepwise extracellular vesicles (EVs) isolation from porcine follicular fluid, their further characteristic and proteomic analysis by tandem mass tag (TMT)-labeled liquid chromatography-tandem mass spectrometry (LC-MS/MS).

2.6. Electrophoretic light scattering

Zeta potential measurements were conducted utilizing a Zetasizer Nano instrument (Malvern Panalytical Ltd). The ELS technique was employed, whereby particles in a liquid suspension are subjected to an electric field. Upon exposure, charged particles are moving at a distinctive velocity known as electrophoretic mobility, which can be recalculated into zeta potential.

2.7. Flow cytometry

To confirm the expression of typical EV marker proteins, the FF-EVs were analyzed with the high-resolution FC as previously described [30]. Each EV-enriched sample was stained with mouse monoclonal allophycocyanin (APC)-conjugated antibodies against CD63 (clone MEM-259; Thermo Fisher Scientific, Wilmington, DE, USA) and CD81 (clone 5A6; BioLegend, San Diego, CA, USA) or the appropriate isotype control (mouse IgG1 k APC, Miltenyi Biotec, Bergisch Gladbach, Germany). Prior to staining, antibodies were suspended in DPBS without Ca^{2+} and Mg^{2+} (Sigma-Aldrich) and centrifuged at 21000 $\times g$ for 20 min at 4°C to eliminate potential debris and protein aggregates. Next, supernatants were mixed with EV-enriched samples in new tubes and incubated for 20 min at 4°C. The analysis was performed with an Apogee A60-Micro-PLUS (Apogee Flow Systems, Hemel Hempstead, UK) and the percentage of gated positive events was calculated by Histogram software v242 (Apogee Flow Systems). Control samples (without the FF-EVs) were also acquired to confirm the absence of potential background particles.

2.8. Protein digestion

Sample preparation and proteomic analysis were performed in the Mass Spectrometry Laboratory of the Institute of Biochemistry and Biophysics Polish Academy of Sciences.

Each FF-EV sample was suspended in 120 μL of lysis buffer containing 5 % trifluoroethanol (TFE) and 50 mM triethylammonium bicarbonate (TEAB) in PBS. Lysis was performed by 30 min sonication in ultrasound bath followed by 1 h vortex. Protein concentration was measured using Pierce BCA Protein Assay Kit (Thermo Fisher Scientific). To 30 μg of proteins from each sample in equal lysis buffer volumes 1 M TEAB buffer was added to a concentration of 100 mM. Cysteines were reduced by 1 h incubation in 60 ℃ with 5 mM Tris(2-carboxyethyl) phosphine (TCEP), followed by the reaction with 15 mM methyl methanethiosulfonate (MMTS). Proteins digestion was performed overnight in 37 ℃ with 1.2 μg of trypsin (Promega, Madison, WI, USA). The final concentration of TFE during digestion was 4 %. Peptides were labelled with TMTpro 16plex tags (Thermo Fisher Scientific) in 40 μL acetonitrile (ACN) for 1 h on vortex. The reaction was quenched by the addition of 8 μL 5 % hydroxylamine. After checking the labelling efficiency, peptides were combined and desalted using four 30 mg Oasis HLB columns (Waters, Milford, MA, USA). Briefly, cartridges were preconditioned with 1 mL methanol and washed with 1 mL 1.5 % ACN and 0.1 % formic acid (FA). After sample loading and rinsing with 1 mL 1.5 % ACN and 0.1 % FA, peptides were eluted from columns with 300 μL 90 % ACN and 0.1 % FA. Eluates from three columns were pulled together, dried in SpeedVac, resuspended in 500 μL 10 mM ammonium hydroxide with 2 % ACN and further used for high pH offline fractionation. Fourth eluate was dried, resuspended in 1 % FA in water and used for FAIMSpro online fractionation.

2.9. Reversed-phase peptide fractionation at high pH (HpRP) for LC-MS/MS

Mixed labelled peptides were fractionated using high-pH reverse-phase chromatography (HpRP) on a XBridge Peptide BEH C18 column (4.6 ×250 mm, 130 Å, 5 μm; Waters). Separation was carried out at 0.8 mL/min flow rate for 50 min using the Waters Acquity UPLC H-class system. Mobile phases consisted of water (A), ACN (B) and 100 mM ammonium hydroxide solution (C). The percentage of phase C was remained constant at 10 % through the entire gradient. Fractions were collected every 1 min starting from second minute of the run. The following gradient was applied: 3–8 % solvent B for 2 min, 8–15 % for 8 min, 15–25 % for 17 min, 25–33 % for 8 min, 33–50 % for 7 min, 50–90 % for 4.5 min, 1.5 min isocratic hold at 90 % and the final column equilibration at 3 % phase B for 2 min. The peptide elution profile was monitored at 214 nm. 48 fractions were dried in Speedvac and reconstituted in Evosep solvent A (0.1 % FA in water) by 30 min vortex and sonication, respectively. Samples were concatenated by mixing

every 24th fraction.

2.10. LC-MS/MS analysis

HpRP fractions were analyzed using LC-MS system composed of Evosep One (Evosep Biosystems, Odense, Denmark) directly coupled to a Orbitrap Exploris 480 mass spectrometer (Thermo Fisher Scientific). Unfractionated peptides were measured by the same LC-MS system with ion mobility separation carried out using FAIMSpro interface (ThermoFisher Scientific). Samples were loaded onto disposable Evotips C18 trap columns (Evosep Biosystems) and chromatography for HpRP fractions was carried out as described previously [29]. Non-fractionated peptides were separated at a flow rate 220 mL/min for 88 min (Evosep Extended method, 15 samples per day). Data was acquired in positive mode with a data-dependent method using the following parameters. MS1 resolution was set to 60000 with a normalized automatic gain control target at 300 %, auto maximum inject time and a scan range of 300–1700 *m/z*. For MS2, resolution was set at 30000 with a standard normalized automatic gain control target, auto maximum inject time and top 25 precursors within an isolation window of 1.2 *m/z* considered for MS/MS analysis. Dynamic exclusion was set at 20 s with allowed mass tolerance of ± 10 ppm, the precursor intensity threshold at 5e3 and precursor fit threshold at 70 %. Precursor were fragmented in higher-energy collisional dissociation mode with normalized collision energy of 30 %. TurboTMT resolution mode was set to "TMTpro Reagents". The pray voltage was set to 2.1 kV, funnel radiofrequency level to 40, and heated capillary temperature to 275°C.

Non-fractionated sample was measured six times, using multi-FAIMS compensation voltage (CV) methods with 3 CV values for each run (-35, −50, −65; −37.5, −52.5, −67.5; −40, −55, −70; −42.5, −57.5, −72.5; −45, −60, −75; −47.5, −62.5, −80, respectively). Cycle time was set to 1 s for every CV value, the rest of mass spectrometry parameters was as described above.

2.11. Bioinformatic analysis

Each file derived from FAIMSpro measurement was converted into a series of mzXML files (one per each CV value) FAIMS MzXML Generator (https://github.com/PNNL-Comp-Mass-Spec/FAIMS-MzXML-Generator). These files along with raw data originating from standard measurements were submitted into MaxQuant/Andromeda software suite (version 2.0.1.0) [31] using *Sus scrofa* Swissprot database (version 2023_01, https://www.uniprot.org/) and MaxQuant contaminants database. The search included tryptic-generated peptides, metylthio (C) was set as a fixed modification and oxidation (M) as a variable one. Reporter MS2 TMTpro 16-plex quantification was specified in order to obtain values for quantitative analysis. Reverse database was used for target/decoy statistical results validation, peptide and protein false discovery rate (FDR) was set to 0.01. Isobaric match between runs function was enabled. The MS data are available in ProteomeXchange Consortium via the PRIDE partner repository with the dataset identifier PXD054450 and https://doi.org/10.6019/PXD054450.

Protein groups along with their quantitative data were further analyzed in R Studio (version 4.2.2) using the Bioconductor "DEP" package (version 1.23.0) as extensively described at https://bioconductor.org/packages/devel/bioc/vignettes/DEP/inst/doc/DEP.html. Hits from reversed database, proteins identified only by site, repeated and duplicated proteins, and contaminants were excluded from the dataset. Only proteins with an identified minimum of two peptides per protein were used for the analysis of differentially abundant proteins (DAPs). DAPs were determined based on an adjusted *p*-value (*q*-value) using the multiple testing corrected by the Benjamini-Hochberg correction with FDR of less than 0.05 and a fold change (FC) cut-off of ± 1.5. Proteomic data visualization was performed by the R package "ggplot2" and GraphPad Software (La Jolla, CA, USA). Following the results of principal component analysis, one outlier sample was removed from each treated group. Thus, further functional analyses of DAPs were performed using three biological replicates ($n = 3$) (Fig. S1). A Venn diagram was constructed at https://bioinformatics.psb.ugent.be/webtools/Venn/.

2.12. Functional analysis of DAPs

Functional enrichment analyses based on Gene Ontology (GO) and Kyoto Encyclopedia of Genes and Genomes (KEGG) databases were performed by KOBAS-i software (version 3.0, http://kobas.cbi.pku.edu.cn/) [32]. To identify DAPs significantly enriched in GO terms or KEGG pathways, analyses were conducted using *Sus scrofa* database and enrichment analysis was carried out using the ORA (overrepresentation analysis) method with hypergeometric test and Fisher's exact test with Benjamini-Hochberg FDR correction (q-value < 0.05).

Additionally, to better understand DAPs functions, identification and characterization of protein-protein interactions (PPIs) were also performed by the Search Tool for the Retrieval of Interacting Genes (STRING) database (version 12.0, https://string-db.org/) [33]. PPIs were determined with a minimum required interaction score of 0.4.

2.13. Statistical analysis

Statistical significance was calculated using GraphPad Software version 8.0 (La Jolla, CA, USA). To verify the distribution of data, the Shapiro-Wilk test was performed. Due to the normal distribution of data, the parametric one-way ANOVA followed by Tukey's *post hoc* test was used and differences were considered statistically significant when $p < 0.05$. All data are presented as mean ± standard deviation (SD).

3. Results

3.1. Characteristic of FF-EVs

The obtained FF-EV-enriched samples were analyzed according to particles morphology, concentration, size range and zeta potential. In all examined groups, TEM analysis revealed the presence of particles with typical "cup-shape" vesicular morphology without any signs of the damage (Fig. 2). NTA analysis showed that the FF-EVs size distribution ranged between 50 and 450 nm in all examined groups. However the majority of particles was under 250 nm in diameter (Fig. 3A).

Additionally, NTA results indicated significantly lower ($p < 0.05$) particle concentration in the I group ($8.6 \times 10^{11} \pm 7.9 \times 10^{10}$/mL) when compared to the VD ($1.4 \times 10^{12} \pm 1.6 \times 10^{11}$/mL) and VD+I ($1.5 \times 10^{12} \pm 3.4 \times 10^{11}$/mL) groups. No significant differences in total FF-EVs concentration were found in comparison to the C group ($1.3 \times 10^{12} \pm 9.1 \times 10^{10}$/mL) (Fig. 3B). In the I and VD+I groups, modal particles diameter was markedly smaller ($p < 0.05$) when compared to the VD group (134 ± 12.2 nm, 134 ± 2.52 nm, 158 ± 9.89 nm, respectively). The average modal size of the FF-EVs from the C group was 143 ± 3.18 nm (Fig. 3C).

VD and I, acting alone or in combination, did not affect the FF-EVs zeta potential, which was less than – 20 mV in all examined groups (Fig. 3D).

3.2. Analysis of FF-EVs protein markers

The FF-EV samples were phenotypically characterized by high-resolution flow cytometry to determine the presence of EV-specific surface tetraspanins - CD63 and CD81 (Fig. 4). This analysis demonstrated $CD63^+$ and $CD81^+$ subpopulations of the FF-EVs in all examined groups with the characteristic profile: $CD81^+ > CD63^+$. In the C group, 23.5 ± 11.6 % of particles were $CD63^+$ and 49.1 ± 4.97 % were $CD81^+$. After VD, I and VD+I treatment, the abundance of CD63-bearing (Fig. 4A, A'; 19.4 ± 10.2 %, 17.0 ± 6.95 %, and 17.1 ± 9.93 %, respectively) and CD81-bearing (Fig. 4B, B'; 49.9 ± 2.06 %, 51.4 ± 5.14 %, and 37.1 ± 13.1 %, respectively) FF-EVs were unchanged.

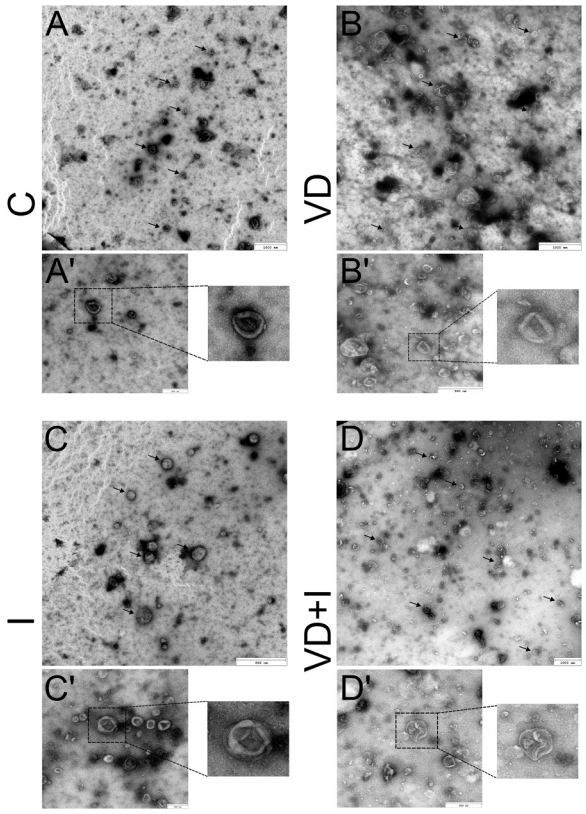

Fig. 2. Transmission electron microscopy (TEM) visualization of follicular fluid-derived extracellular vesicles (FF-EVs) isolated from porcine ovarian follicles cultured *in vitro* of control (C) (A, A'), vitamin D_3 (VD) (B, B'), insulin (I) (C, C'), and both vitamin D_3 and insulin (VD+I) (D, D') treated groups. Representative wide field (A, B, C, D) and close-up (A', B', C', D') TEM images of FF-EV-enriched samples from each experimental group. Black arrows indicate "cup-shaped" vesicular morphology.

In addition to results demonstrated by flow cytometry, we have also confirmed the presence of CD63 and CD81 proteins in the porcine FF-EVs using LC-MS/MS analysis. Overall, we have demonstrated the expression of 88 out of 100 EV-specific marker proteins in all experimental groups (Table S1) according to the MISEV guidelines and Vesiclepedia [36,37].

3.3. Identification of DAPs in FF-EVs

To reveal changes in the proteome of the FF-EVs after VD, I, and VD+I treatment, a quantitative proteomic analysis was conducted using TMT labeling LC-MS/MS method that allowed to identify 3976 proteins in each FF-EV sample. Following appropriate filters application (proteins identified only by site, repeated and duplicated proteins, and contaminants were removed), 2766 proteins underwent further comparative proteomic analysis in R software (Table S2).

In the FF-EVs, 48 DAPs were identified between examined groups by setting a q-value below 0.05 and a FC cut-off of $\pm$ 1.5 as the arbitrary threshold (Table S3, Table 1). The greatest number of DAPs were found in the comparisons VD *vs* C and I *vs* C (19 and 16 DAPs, respectively). Among DAPs identified in the VD *vs* C group, 10 DAPs were up-regulated and 9 DAPs were down-regulated, while in the I *vs* C group, 4 DAPs were up-regulated and 12 DAPs were down-regulated (Fig. 5A). Furthermore, LC/MS-MS analysis showed 8 DAPs (4 up-regulated and 4 down-regulated) in the VD+I *vs* C group, 8 DAPs (3 up-regulated and 5 down-regulated) in the VD *vs* VD+I group and 10 DAPs (6 up-regulated and 4 down-regulated) in the I *vs* VD+I group (Fig. 5A). Volcano plots show a direct distribution of all identified DAPs (Fig. 5B-F), while a heatmap their hierarchical clustering across experimental conditions (Fig. 5H). Interestingly, the most of DAPs were unique to their respective groups. A Venn diagram illustrates that 14, 12, 2, 5 and 6 proteins were uniquely detected in the VD *vs* C, I *vs* C, VD+I *vs* C, VD *vs* VD+I and I *vs* VD+I groups, respectively (Fig. 5G). Among all DAPs, 2 identical proteins were found in three comparisons: RPL36A in VD *vs* C, VD+I *vs* C, I *vs* VD+I groups and COL5A3 in VD+I *vs* C, VD *vs* VD+I, I *vs* VD+I groups. Moreover, only one DAP (PLG) had common change in I *vs* C, VD+I *vs* C, VD *vs* VD+I and I *vs* VD+I groups (Fig. 4G, Table 1).

3.4. GO and KEGG pathways, and STRING functional annotations of DAPs

To evaluate the possible biological functions of DAPs identified in the FF-EVs following VD, I and VD+I treatment, the GO and the KEGG enrichment analyses were performed using KOBAS-i software. Additionally, the STRING database was employed to reveal the functional PPIs network in the comparisons VD *vs* C, I *vs* C and VD+I *vs* C. Due to the low number of DAPs identified in the VD *vs* VD+I and I *vs* VD+I groups, the STRING analysis did not detect PPIs in those groups.

In the comparison VD *vs* C, the DAPs were clustered into 8 unique clusters (Fig. 6A) and were annotated to 47 GO categories and 2 functional KEGG pathways (Table S4). Cluster 1 was the most enriched and involved the following DAPs: RPL36 A, RPL37, RPL21, RPL32, RPL28 (Fig. 6A, B). These proteins were associated with enriched ribosome-related terms such as: "cytosolic large ribosomal subunits" (GO:0022625), "large ribosomal subunits" (GO:0015934), "structural constituent of ribosome" (GO:0003735), and "ribosome" (ssc03010), as well as the terms "cytoplasmic side of rough endoplasmic reticulum membrane" (GO:0098556), "biological process" (GO:0008150) and "molecular function" (GO:0003674) (Fig. 6A-C). The other highly enriched terms and pathways were related to "protein disulfide isomerase activity", "positive regulation of extrinsic apoptotic signaling pathway", "organelle fission", "identical protein binding", "iron ion transport", "negative regulation of protein secretion", "fatty acid binding" and "cell-substrate adhesion". Additionally, these DAPs were assigned as part of the proteins "dendritic spine head", "postsynaptic endocytic zone membrane", "extracellular space" and "endoplasmic reticulum lumen" (Fig. 6C). The STRING analysis of identified DAPs generated a PPI network with 19 nodes and 17 edges (PPI enrichment p-value = 1.83×10^{-8}). It also confirmed the assignment of DAPs by KOBAS-i to 6 GO terms such as "structural constituent of ribosome" (GO:0003735, 5 DAPs, q-value = 0.0115), "endoplasmic reticulum lumen" (GO:0005788, 3 DAPs, q-value = 0.0096), "endoplasmic reticulum" (GO:0005783, 7 DAPs, q-value = 0.0232), "extracellular space" (GO:0005615, 7 DAPs, q-value = 0.0232), "cytoplasmic side of rough endoplasmic reticulum membrane" (GO:0098556, 2 DAPs, q-value = 0.0381) and "cytosolic large ribosomal subunit" (GO:0022625, 4 DAPs, q-value = 0.0031). Two KEGG pathway terms identified by KOBAS-i assignment, "ribosome" (ssc03010, 5 DAPs, q-value = 1.80×10^{-5}) and "protein processing in endoplasmic reticulum" (ssc04141, 3 DAPs, q-value = 0.0466) were also confirmed by the STRING analysis (Fig. 6D).

In the comparison I *vs* C, the DAPs were clustered into 12 unique clusters (Fig. 7A) and were assigned to 75 GO and 8 KEGG pathway terms (Table S4). Cluster 3 was the most enriched and contained the following DAPs: ERP29, CALR, PDIA3, THBS3, PPIB, TTR, MYDGF and MANF (Fig. 7A, B). These DAPs indicated an enrichment of GO categories associated with protein functional processes such as "protein binding" (GO:0050681), "protein maturation" (GO:0006457), "protein stabilization" (GO:0050821), and "protein localization" (GO:0006611, GO:0034504). Additionally, they were also involved in "cell migration" (GO:2000510, GO:1901164, GO:0010595), "cell cycle" (GO:0071157, GO:0040020, GO:0071157), and "gene expression" (GO:0010628, GO:0017148). Further analysis of the remaining DAPs in this comparison revealed enrichment of pathways involved in "thyroid hormone

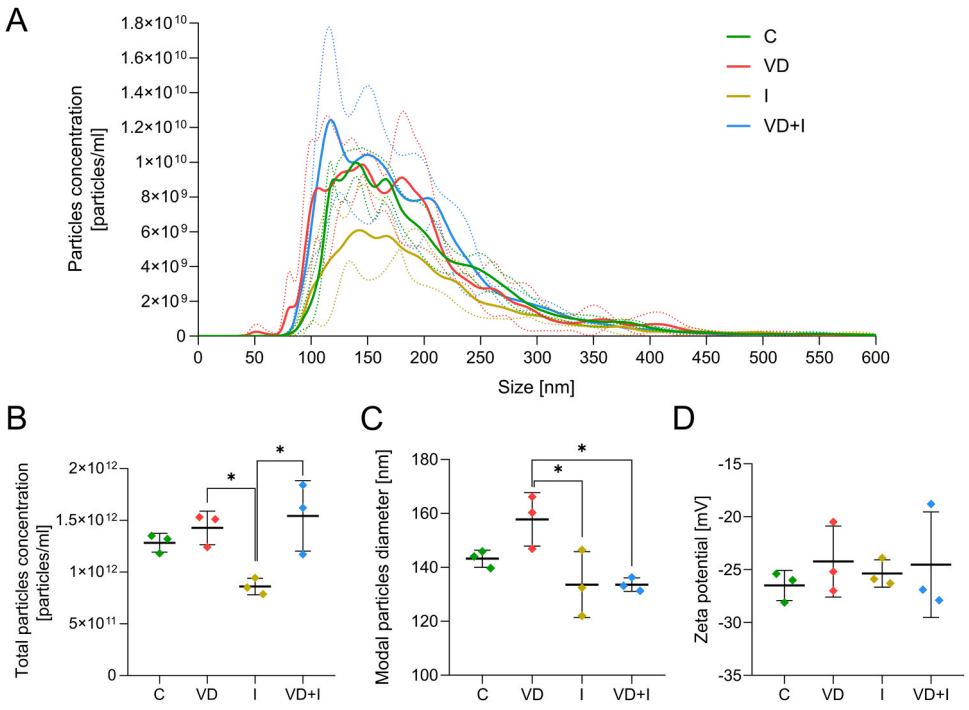

Fig. 3. Characteristic of follicular fluid-derived extracellular vesicles (FF-EVs) from porcine ovarian follicles cultured *in vitro* of control (C), vitamin D_3 (VD), insulin (I), and both vitamin D_3 and insulin (VD+I) treated groups. (A) The profile of particle distribution showing mean size and concentration of FF-EVs in each experimental group (solid lines) with standard deviation (SD) (dotted lines). (B) Total concentration, (C) modal diameter, and (D) zeta potential of FF-EVs in each experimental group presented as the mean ± SD. *$p < 0.05$ (one-way ANOVA followed by Tukey's *post hoc* test) ($n = 3$).

transport", "heterotypic cell-cell adhesion", "regulation of immune response", "scavenger receptor activity", "positive regulation of extrinsic apoptotic signaling pathway" and "cholesterol metabolism" (Fig. 7C). According to the STRING database, the functional classification of produced a PPI network with 16 nodes and 10 edges (PPI enrichment p-value $= 1.17 \times 10^{-5}$) revealed specific clustering of the "MHC class I peptide loading complex" (GO:0042824, 2 DAPs, q-value = 0.0116), "endoplasmic reticulum lumen" (GO:0005788, 5 DAPs, q-value $= 2.19 \times 10^{-6}$) and "extracellular space" (GO:0042824, 7 DAPs, q-value = 0.0116) in agreement with KOBAS-i results (Fig. 7D).

In the VD+I *vs* C comparison, the DAPs were clustered only into 3 unique clusters (Fig. 8A) and were annotated into 26 GO and 11 KEGG enrichment pathways (Table S4). Cluster 1 was the most enriched and contained 3 DAPs: RPL36A, RPL21 and RPS23 (Fig. 8A, B). Two of these proteins (RPL36A and RPL21) were also differentially abundant in the VD *vs* C comparison. The GO and the KEGG enrichment analysis assigned the DAPs from the VD+I *vs* C comparison to "cytosolic large ribosomal subunits" (GO:0022625), "large ribosomal subunits" (GO:0015934), "structural constituent of ribosome" (GO:0003735), "polysomal ribosome" (GO:0042788), and "ribosome" (ssc03010) terms. Additionally, this cluster was expanded by assigning a unique protein (RPS23) for this comparison to the "cytosolic small ribosomal subunit" (GO:0022627), "translation" (GO:0006412), and "stress granule assembly" (GO:0034063) terms (Fig. 8B-C). In the comparison VD+I *vs* C, the functional classification of DAPs generated a PPI network with 8 nodes and 4 edges (PPI enrichment p-value = 0.0281). The DAPs were categorized to "cytoplasmic side of rough endoplasmic reticulum membrane" category (GO:0098556, 2 DAPs, q-value = 0.0421) and "ribosome" category (ssc03010, 3 DAPs, q-value = 0.0029), in agreement with KOBAS-i (Fig. 8D).

In the comparisons VD *vs* VD+I and I *vs* VD+I, the DAPs were clustered into 4 and 7 unique clusters, respectively (Figs. 9A and 10A). In the VD *vs* VD+I group, the 8 identified DAPs were assigned to 11 GO and 1 KEGG pathway terms (Table S4), among which enzyme CYP17A1, playing a crucial role in ovarian steroidogenesis, was identified. CYP17A1 was classified into "hormone biosynthetic process" (GO:0042446), "steroid metabolic process" (GO:0008202), and "glucocorticoid biosynthetic process" (GO:0006704) terms (Fig. 9B, C). Other DAPs were mainly annotated to "regulation of mitotic spindle organization" (GO:0060236, GNAI1), proteolysis (GO:0006508, PLG and CTSF) and "chloride ion binding" (GO:0031404, NPR3) (Fig. 9C). In the I *vs* VD+I comparison, the 10 identified DAPs were enriched in 35 GO and 4 KEGG pathways (Table S4). The most differentially abundant protein in this group was DDX20 assigned into "regulation of steroid biosynthetic process" (GO:0050810), "oogenesis" (GO:0048477) and "histone deacetylase binding" (GO:0042826) terms. Other DAPs were categorized into terms related to "ribosome" (GO:0015934, GO:0022625), "cell communication" (GO:0099527), "protein import into nucleus" (GO:0006607), and "gene expression" (GO:0043484, GO:0070491, GO:0008380, GO:0048255) (Fig. 10C).

4. Discussion

Recently we have found that VD alone or in combination with I modulates the global proteomic profile of granulosa and theca interna cells of the porcine ovarian follicle, influencing the abundance of proteins involved in the regulation of cell proliferation, cell cycle progression, and cholesterol transport [21]. Given that the FF-EVs protein cargo is a part of the entire ovarian follicle proteome, herein we investigated for the first time the effect of VD and/or I on the characteristics and protein composition of the porcine FF-EVs. The present study provides new knowledge about the modulatory role of VD and I on the concentration, size, as well as protein cargo of the porcine FF-EVs, suggesting their impact on the ovarian follicle functions *via* EV-mediated pathway.

In the present study, we confirmed the heterogeneity of the porcine FF-EVs population with the size range between 50 and 450 nm as demonstrated previously [10,29]. Consistently with our recent findings, we noted enrichment of FF samples predominantly with exosomes [29]. The average porcine FF-EVs concentration, diameter, zeta potential and "cup-shaped" morphology were similar to those described in our recent

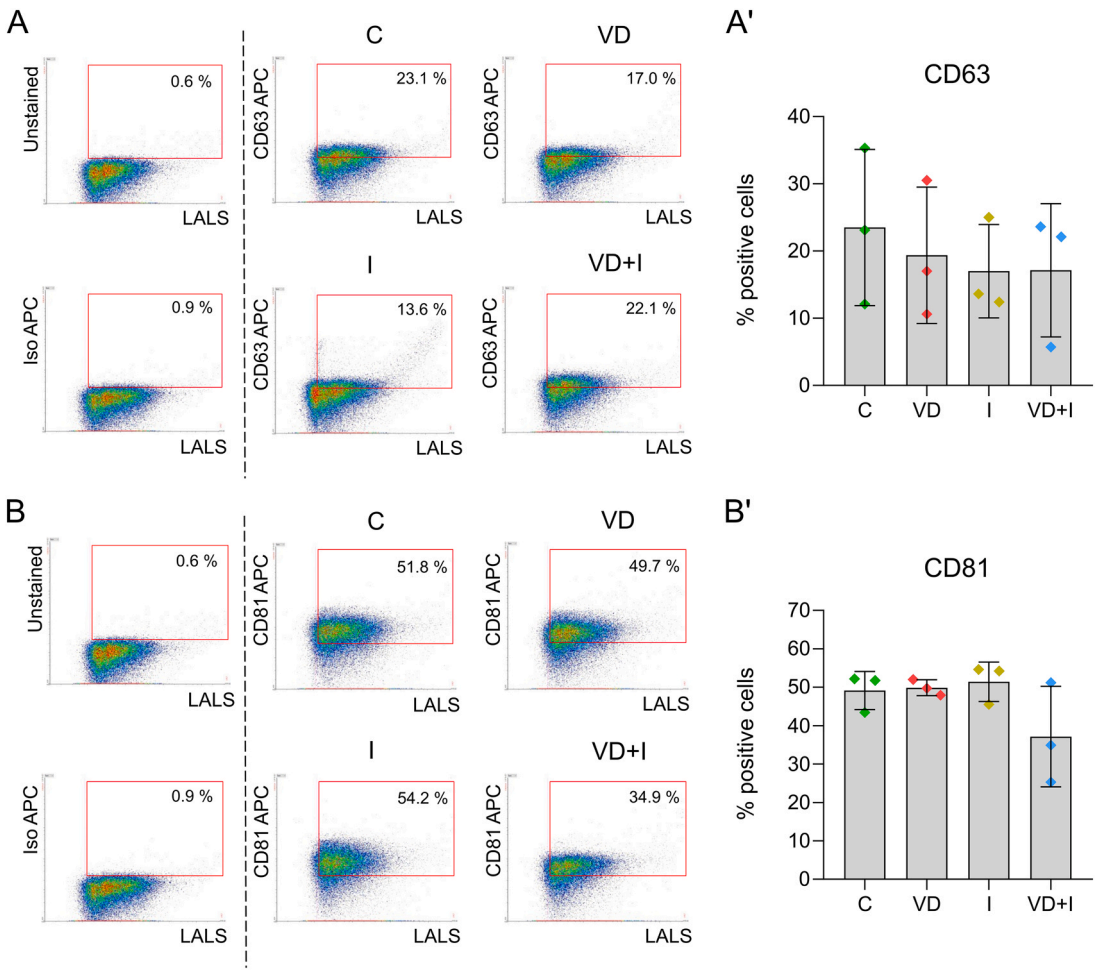

Fig. 4. Flow cytometry representative density plots of follicular fluid-derived extracellular vesicles (FF-EVs) stained with fluorescent anti-CD63 (A, A') and anti-CD81 (B, B') antibodies obtained from porcine ovarian follicles cultured *in vitro* of control (C), vitamin D_3 (VD), insulin (I), and both vitamin D_3 and insulin (VD+I) treated groups. The percentage of positive FF-EVs for the analyzed markers is depicted in red gates with the gating strategy including the APC isotype and unstained control. The percentage of CD63 (A') and CD81 (B') positive FF-EVs is presented as mean values ± standard deviation (SD) (one-way ANOVA followed by Tukey's *post hoc* test) ($n = 3$).APC, allophycocyanin; LALS, large angle light scatter parameter, corresponding to the relative size of analyzed particles.

study [29]. Regarding VD and I impact on the particle characteristics, there were no differences between groups in the FF-EVs phenotype evidenced by unchanged surface CD63 and CD81 expression, as well as colloidal stability in solution marked by unaltered zeta potential. In addition, the sole VD or I treatment did not change the FF-EVs number and size in comparison the control group. Our findings supports previous data on 3T3-L1 adipocytes, showing that neither VD [34] nor I [35] impact the size and number of secreted EVs. On the other hand, we have found that I reduced total FF-EVs concentration and size in comparison to the VD group, whereas the I and VD concomitant treatment withdrawn only the effect on the particle concentration. These findings indicate the plausible role of VD and I interactions in the EV secretory pathway. Our recent proteomic study has shown that EV biogenesis can be modulated by VD and I treatment in the porcine granulosa cells through the effect on Rab27b protein abundance. In details, Rab27b was down-regulated in the VD+I group when compared to the control and VD groups [21]. The Rab27b protein together with other Rab GTPases (Rab2b, Rab9a, Rab5a, and Rab27a) controls exosome biogenesis pathway [36]. The knockdown of Rab27b resulted in multivesicular bodies (MVBs) redistribution towards the perinuclear region in HeLa cells, while its isoform Rab27a silencing reduced membrane docking of MVBs and increased their size. Nonetheless, the inhibited exosome release was observed only after silencing of Rab27a and Rab27b effectors - Slp4 and Slac2b, indicating the complexity of molecular mechanism underlying EV secretion [36]. To the best of our knowledge, this is the first report showing that VD and I interaction seems to impact EV release within porcine ovarian follicle. However it needs further elucidation.

The results of our in-depth proteomic analysis showed for the first time that VD and I alone or in combination could modify the porcine FF-EVs cargo composition. Greater amount of DAPs was identified following VD (19 DAPs) and I (16 DAPs) treatment alone than together (8 DAPs), indicating more pronounced independent effect of those factors on the FF-EVs proteome. By this time, VD was shown to modulate miRNA [37] and lipid [34] composition of adipocyte-derived EVs in the context of inflammation, whereas its effect on EV protein content has never been investigated. Herein, the enrichment analysis of DAPs identified in the VD *vs* C comparison revealed that GO terms related to "large ribosomal subunit", "ribosome" and "cytoplasmic side of rough endoplasmic reticulum membrane" were significantly overrepresented. In this comparison, VD down-regulated large ribosomal subunit proteins (RPL21, RPL28, RPL32, and RPL36A) and ribosomal protein L37 (RPL37). Likewise, among DAPs identified in the comparison VD+I *vs* C, we showed diminished abundance of RPL21, RPL23, and RPL36A proteins, which displayed strong PPIs. Despite ribosomal proteins are known to maintain ribosome structure and catalyze protein biosynthesis, many of them are proposed to have extra-ribosomal functions [38]. Their presence in the EV cargo is not surprising; ribosomal proteins

Table 1
List of differentially abundant proteins (DAPs) identified in follicular fluid-derived extracellular vesicles of porcine ovarian follicles cultured *in vitro* from control (C), vitamin D_3 (VD), insulin (I), and both vitamin D_3 and insulin (VD +I) treated groups.Gene names, full protein names, *q*-values and fold change of each DAPs are included in the table. DAPs were identified through R analysis of LC-MS/MS data using parameters including *q*-values < 0.05 and fold change $\leq$ -1.5 or ≥ 1.5.

	Gene name	Protein name	Changes	q-value	Fold change
VD *vs* C					
1.	MX1	Interferon-induced GTP-binding protein Mx1	Down	0.0497	−2.35
2.	RPL37	Ribosomal protein L37	Down	0.0268	−1.99
3.	RPL21	Large ribosomal subunit protein eL21	Down	0.0005	−1.91
4.	PDIA6	Protein disulfide-isomerase A6	Down	0.0225	−1.80
5.	RPL36A	Large ribosomal subunit protein eL42	Down	0.0028	−1.74
6.	RPL32	Large ribosomal subunit protein eL32	Down	0.0120	−1.59
7.	RPL28	Large ribosomal subunit protein eL28	Down	0.0170	−1.59
8.	ERP29	Endoplasmic reticulum resident protein 29	Down	0.0368	−1.52
9.	PDIA3	Protein disulfide-isomerase A3	Down	0.0309	−1.52
10.	SAA2	Serum amyloid A−2 protein	Up	0.0116	2.16
11.	SAA4	Serum amyloid A−4 protein	Up	0.0220	1.99
12.	FTL	Ferritin	Up	0.0113	1.98
13.	APON	Ovarian and testicular apolipoprotein N	Up	0.0155	1.79
14.	FAT2	FAT atypical cadherin 2	Up	0.0185	1.68
15.	SERPIND1	Heparin cofactor 2	Up	0.0177	1.67
16.	MEMO1	Protein MEMO1	Up	0.0241	1.65
17.	AFM	Afamin	Up	0.0105	1.65
18.	MSTN	Growth/differentiation factor 8	Up	0.0119	1.58
19.	FBN2	Fibrillin 2	Up	0.0127	1.52
I *vs* C					
1.	SOD2	Superoxide dismutase [Mn], mitochondrial	Down	0.0202	−1.81
2.	TPP2	Tripeptidyl-peptidase 2	Down	0.0009	−1.77
3.	PLG	Plasminogen	Down	0.0025	−1.72
4.	PPIB	Peptidyl-prolyl cis-trans isomerase	Down	0.0005	−1.71
5.	ETFA	Electron transfer flavoprotein subunit alpha	Down	0.0025	−1.67
6.	CALR	Calreticulin	Down	0,0201	−1.61
7.	MANF	Mesencephalic astrocyte derived neurotrophic factor	Down	0.0027	−1.55
8.	MYDGF	Myeloid derived growth factor	Down	0,0283	−1.52
9.	PDIA3	Protein disulfide-isomerase A3	Down	0.0112	−1.52
10.	CD200	CD200 molecule	Down	0.00004	−1.51
11.	RPL30	Large ribosomal subunit protein eL30	Down	0.0412	−1.51
12.	ERP29	Endoplasmic reticulum resident protein 29	Down	0.0186	−1.50
13.	PRG4	Proteoglycan 4	Up	0.0003	3.41
14.	THBS3	Thrombospondin 3	Up	0.0021	1.69
15.	LDLRAP1	Low density lipoprotein receptor adaptor protein 1	Up	0.0172	1.58
16.	TTR	Transthyretin	Up	0.0235	1.51
VD+I *vs* C					
1.	ORM1	Alpha−1-acid glycoprotein	Down	0.0207	−2.62
2.	RPL36A	Large ribosomal subunit protein eL42	Down	0.0196	−1.81
3.	RPL21	Large ribosomal subunit protein eL21	Down	0.0483	−1.79
4.	RPS23	Small ribosomal subunit protein uS12	Down	0.0455	−1.55
5.	PLG	Plasminogen	Up	0.0000004	2.89
6.	THBS3	Thrombospondin 3	Up	0.0023	2.10
7.	COL5A3	Collagen type V alpha 3 chain	Up	0.0025	1.97
8.	ADIPOQ	Adiponectin	Up	0.0341	1.82
VD *vs* VD+I					
1.	PLG	Plasminogen	Down	0.0000000000006	−3.76
2.	GNAI1	Guanine nucleotide-binding protein G(i) subunit alpha−1	Down	0.0340	−2.57
3.	CTSF	Cathepsin F	Down	0.0127	−1.69
4.	SH3BP1	SH3 domain binding protein 1	Down	0.0126	−1.52
5.	COL5A3	Collagen type V alpha 3 chain	Down	0.0242	−1.51
6.	SAA2	Serum amyloid A−2 protein	Up	0.00004	2.51
7.	NPR3	Natriuretic peptide receptor 3	Up	0.0187	1.69
8.	CYP17A1	Steroid 17-alpha-hydroxylase/17,20 lyase	Up	0.0452	1.63
I *vs* VD+I					
1.	PLG	Plasminogen	Down	0.0000000000006	−4.99
2.	COL5A3	Collagen type V alpha 3 chain	Down	0.0021	−1.73
3.	ADIPOQ	Adiponectin	Down	0.0105	−1.67
4.	ITIH5	Inter-alpha-trypsin inhibitor heavy chain 5	Down	0.0039	−1.62
5.	DDX20	RNA helicase	Up	0.0028	1.91
6.	MKLN1	Muskelin 1	Up	0.0077	1.68
7.	KPNA2	Importin subunit alpha	Up	0.0019	1.63
8.	RPL36A	Large ribosomal subunit protein eL42	Up	0.0172	1.59
9.	CENPV	Centromere protein V	Up	0.0318	1.55
10.	FUS	FUS RNA binding protein	Up	0.0314	1.53

and their transcripts were demonstrated in the FF-EVs of cows [39] and horses [40], respectively. Furthermore, Matsuno et al. [41] identified transcripts encoding ribosomal proteins in the porcine FF-EVs. They also demonstrated the presence of full-length mRNAs, which may be translated into ribosomal proteins and contribute to cell-to-cell communication within the porcine follicle. Considering the role of ribosomal proteins enriched in EVs, they are proposed to participate in RNA binding, sorting or degradation [42]. The RPL36, identified also in

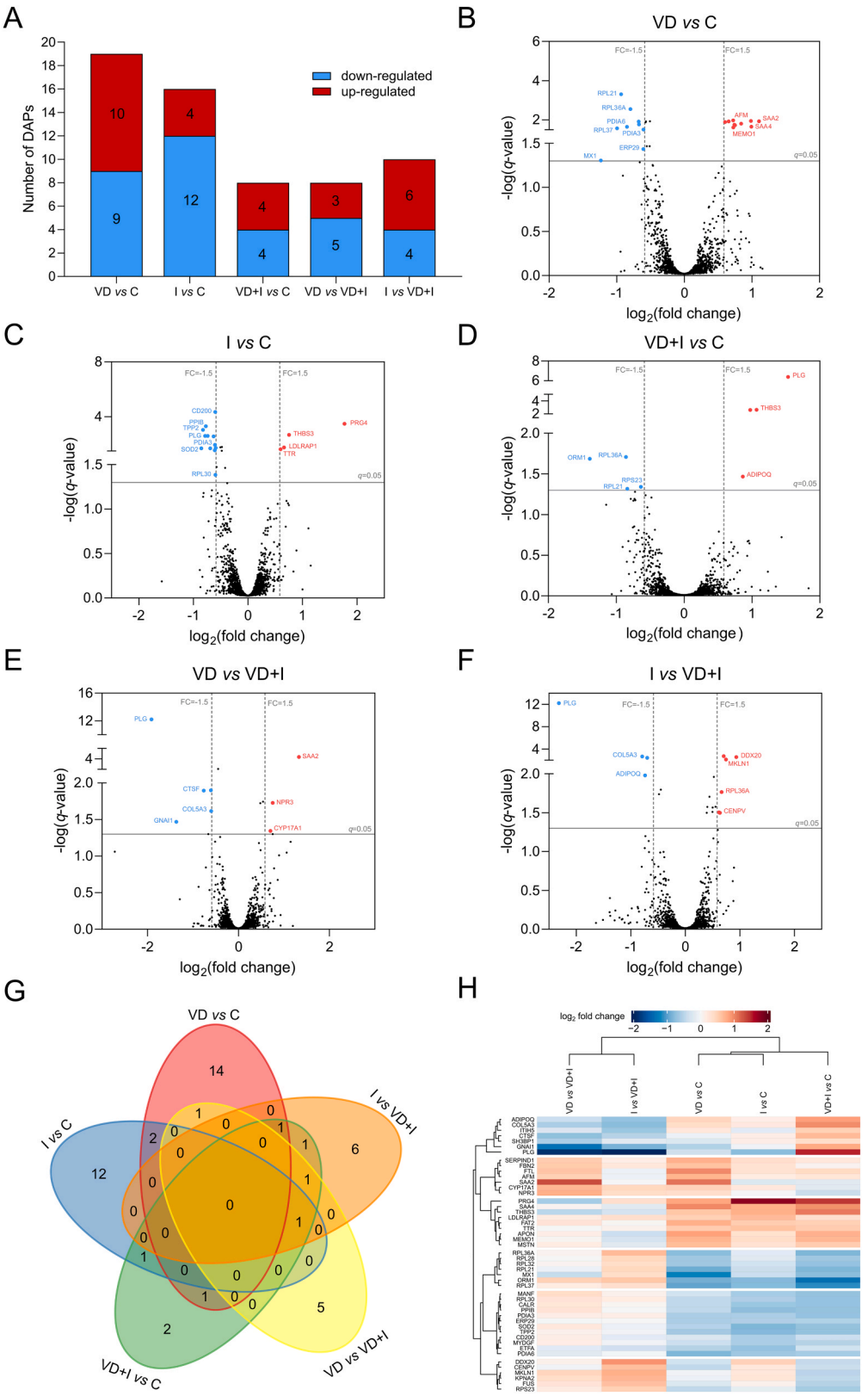

Fig. 5. Protein profile of differentially abundant proteins (DAPs) in follicular fluid-derived extracellular vesicles (FF-EVs) from porcine ovarian follicles cultured *in vitro* from control (C), vitamin D_3 (VD), insulin (I), and both vitamin D_3 and insulin (VD+I) treated groups. (A) Total numbers of up- and down-regulated DAPs determined in VD *vs* C, I *vs* C, VD+I *vs* C, VD *vs* VD+I and I *vs* VD+I groups. (B-F) Volcano plot representations of DAPs [fold change ≤ -1.5 and ≥ 1.5; *q*-value < 0.05] showing the distribution of significance [$-\log$(*q*-value)] *vs* fold change [log2(fold change)] for all identified proteins between examined groups. (G) Venn diagram illustrated the specific and overlap of DAPs, and (H) heatmap and hierarchical clustering analysis depicted the expression patterns of DAPs between VD *vs* C, I *vs* C, VD+I *vs* C, VD *vs* VD+I and I *vs* VD+I groups. Down-regulated DAPs are marked in blue and up-regulated DAPs are marked in red.

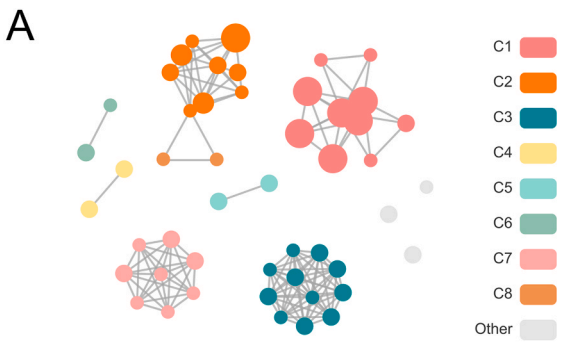

B

Cluster	Proteins
C1	RPL36A, RPL37, RPL21, RPL32, RPL28
C2	PDIA6, PDIA3, ERP29, RPL21
C3	MX1
C4	AFM, MSTN, PDIA3, SERPIND1, MX1
C5	SAA2, SAA4
C6	FTL
C7	MSTN
C8	ERP29
Other	FAT2, AFM, RPL37

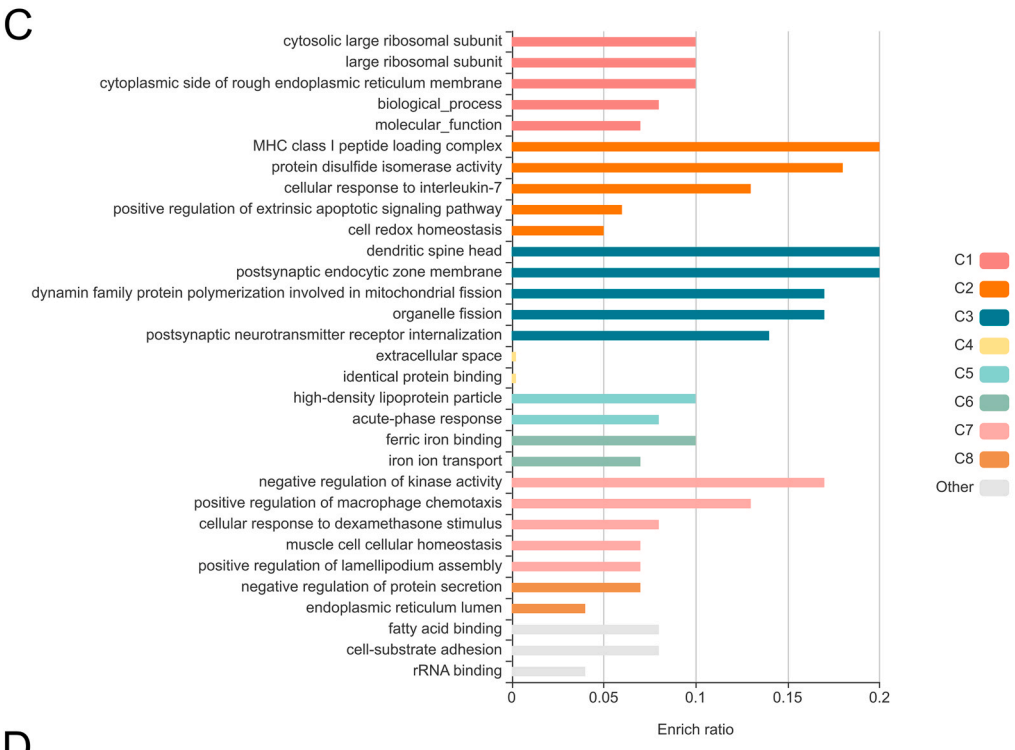

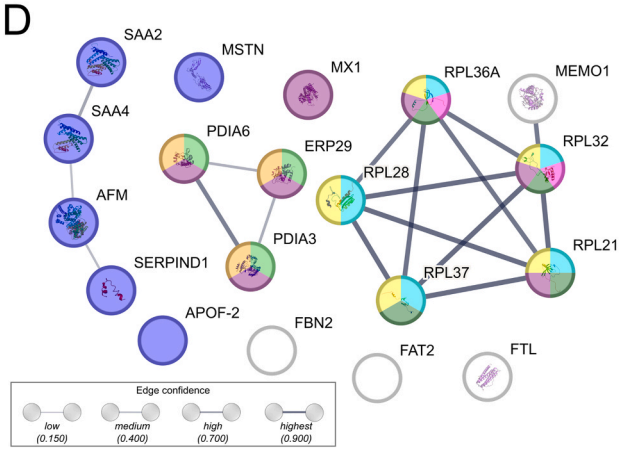

Colour of nodes	GO-term	Description	FDR
	GO:0003735	Structural constituent of ribosome	0.0115
	GO:0005788	Endoplasmic reticulum lumen	0.0096
	GO:0005783	Endoplasmic reticulum	0.0232
	GO:0005615	Extracellular space	0.0232
	GO:0098556	Cytoplasmic side of rough endoplasmic reticulum membrane	0.0381
	GO:0022625	Cytosolic large ribosomal subunit	0.0031
	ssc03010	Ribosome	1.80E-05
	ssc04141	Protein processing in endoplasmic reticulum	0.0466

Fig. 6. Summary of functional annotation and pathway enrichment analysis of differentially abundant proteins (DAPs) evaluated in the VD *vs* C group. (A) cirFunMap visualization of gene-list enrichment results into unique clusters. Each node represents an enriched term with color corresponding to the unique cluster according to term identity, while each edge represents a significant correlation between terms. (B) The table shows a list of proteins present in the corresponding clusters. (C) The bar chart represents the enriched terms found within each cluster (by color) and the bar length indicates the enrich ratio, calculated as "input gene number"/"background gene number". For each clusters, where numerous terms are enriched, only the top five with the highest enrich ratio are displayed. Detailed associations and annotations of all proteins to GO and KEGG pathway terms in this analysis are provided in Table S4. (D) STRING analysis of predicted protein-protein interaction networks of DAPs. Nodes represent proteins, while edges indicate their interactions with thickness reflecting interaction confidence. Different colors mark detected protein interactions in the clusters of interest, with detailed information provided in the table on the right.

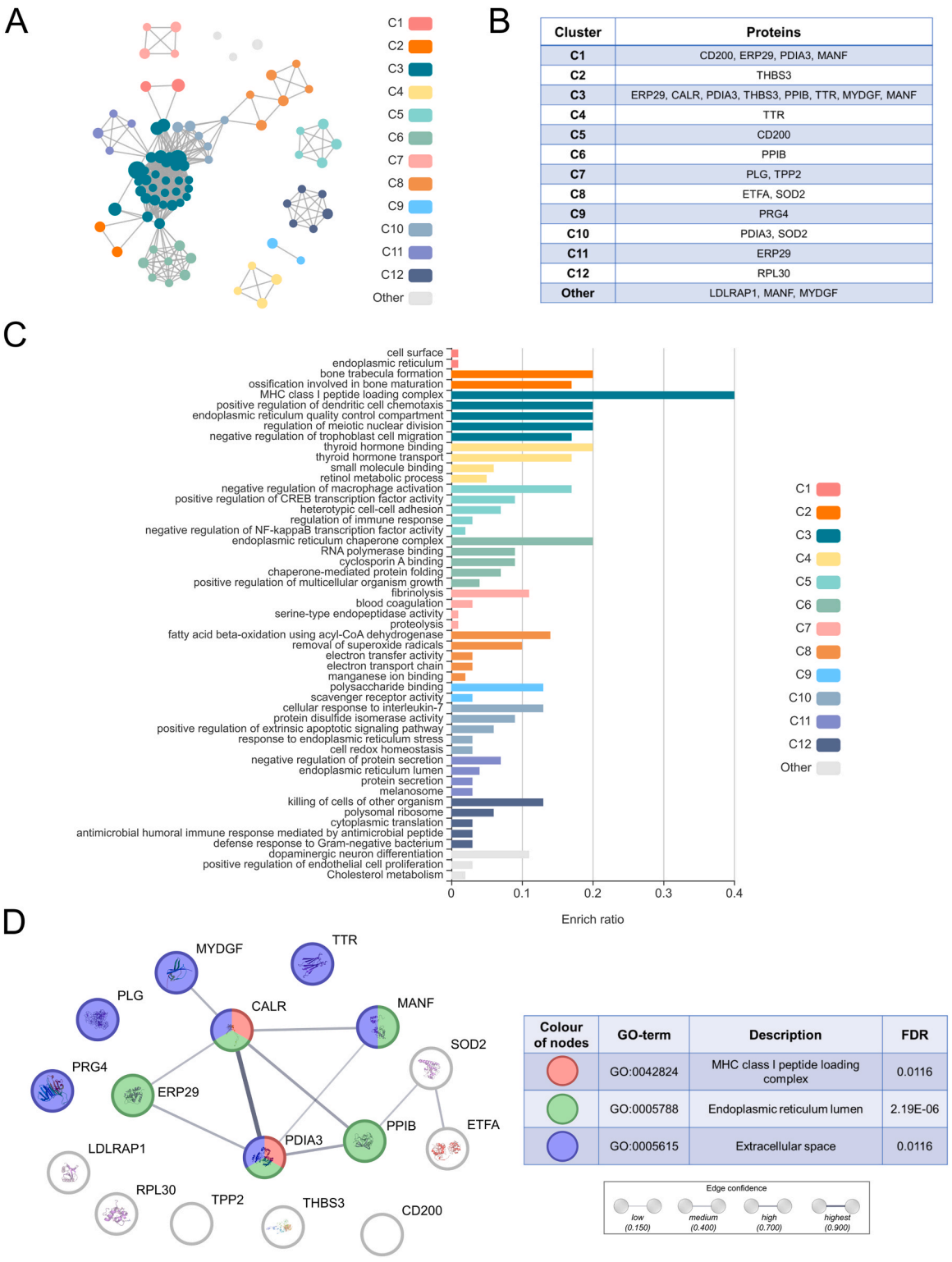

Cluster	Proteins
C1	CD200, ERP29, PDIA3, MANF
C2	THBS3
C3	ERP29, CALR, PDIA3, THBS3, PPIB, TTR, MYDGF, MANF
C4	TTR
C5	CD200
C6	PPIB
C7	PLG, TPP2
C8	ETFA, SOD2
C9	PRG4
C10	PDIA3, SOD2
C11	ERP29
C12	RPL30
Other	LDLRAP1, MANF, MYDGF

Colour of nodes	GO-term	Description	FDR
	GO:0042824	MHC class I peptide loading complex	0.0116
	GO:0005788	Endoplasmic reticulum lumen	2.19E-06
	GO:0005615	Extracellular space	0.0116

Fig. 7. Summary of functional annotation and pathway enrichment analysis of differentially abundant proteins (DAPs) evaluated in the I *vs* C group. (A) cirFunMap visualization of gene-list enrichment results into unique clusters. Each node represents an enriched term with color corresponding to the unique cluster according to term identity, while each edge represents a significant correlation between terms. (B) The table shows a list of proteins present in the corresponding clusters. (C) The bar chart represents the enriched terms found within each cluster (by color) and the bar length indicates the enrich ratio, calculated as "input gene number"/ "background gene number". For each clusters, where numerous terms are enriched, only the top five with the highest enrich ratio are displayed. Detailed associations and annotations of all proteins to GO and KEGG pathway terms in this analysis are provided in Table S4. (D) STRING analysis of predicted protein-protein interaction networks of DAPs. Nodes represent proteins, while edges indicate their interactions with thickness reflecting interaction confidence. Different colors mark detected protein interactions in the clusters of interest, with detailed information provided in the table on the right.

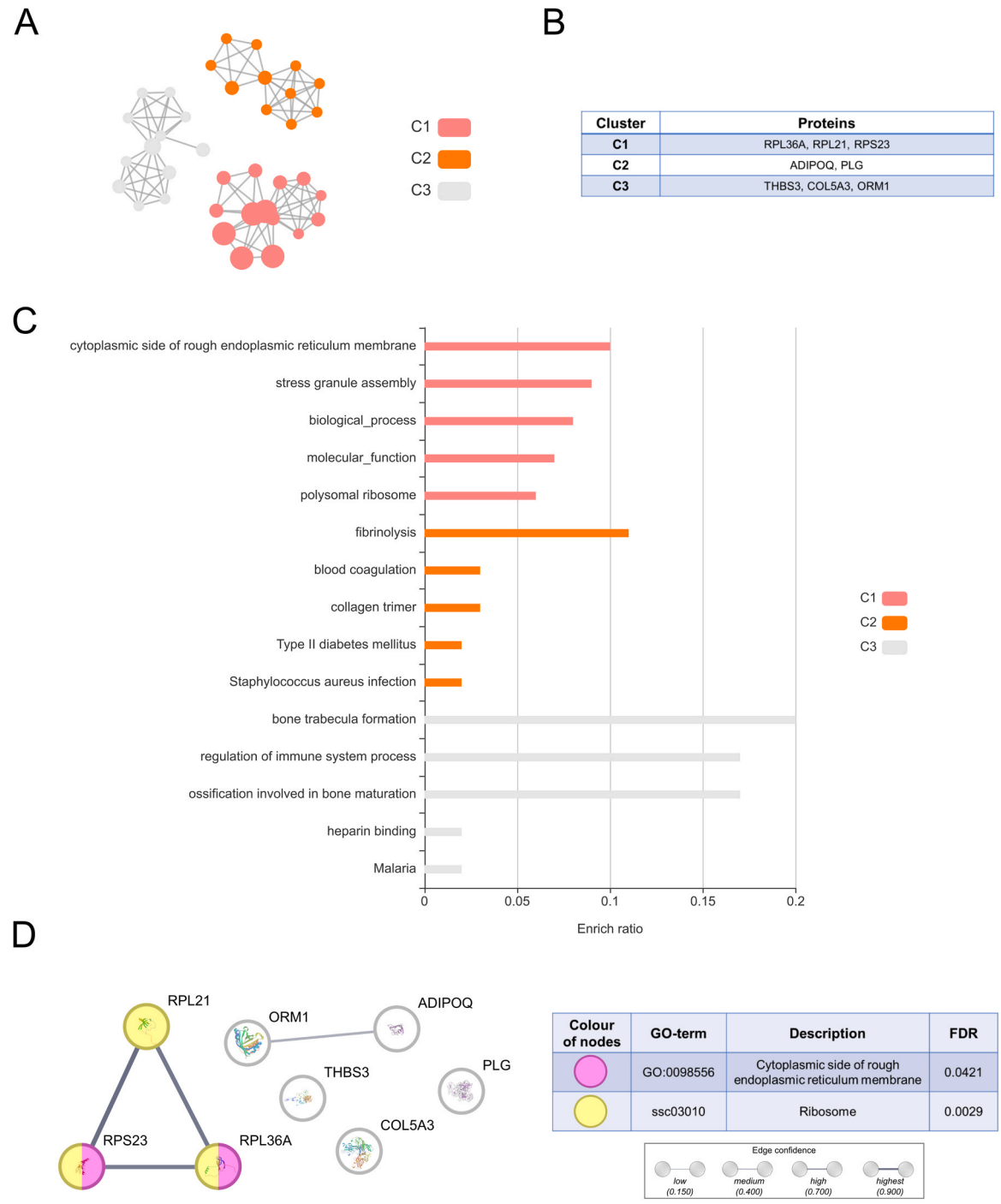

Fig. 8. Summary of functional annotation and pathway enrichment analysis of differentially abundant proteins (DAPs) evaluated in the VD+I *vs* C group. (A) cirFunMap visualization of gene-list enrichment results into unique clusters. Each node represents an enriched term with color corresponding to the unique cluster according to term identity, while each edge represents a significant correlation between terms. (B) The table shows a list of proteins present in the corresponding clusters. (C) The bar chart represents the enriched terms found within each cluster (by color) and the bar length indicates the enrich ratio, calculated as "input gene number"/"background gene number". For each clusters, where numerous terms are enriched, only the top five with the highest enrich ratio are displayed. Detailed associations and annotations of all proteins to GO and KEGG pathway terms in this analysis are provided in Table S4. (D) STRING analysis of predicted protein-protein interaction networks of DAPs. Nodes represent proteins, while edges indicate their interactions with thickness reflecting interaction confidence. Different colors mark detected protein interactions in the clusters of interest, with detailed information provided in the table on the right.

our study, was described as a sorting regulator of EV-carried miR-4432, affecting the crosstalk between endothelial and perivascular cells [43]. Results from epicardial adipose tissue-derived stem cells highlighted the potential of EVs to reprogram the phenotype of recipient cells [44]. Along this line, the ribosomal proteins transferred by FF-EVs could modulate the biological processes within follicular cells. Comprehensive proteomic analysis of bovine ovarian follicles revealed the presence of RPL21 and RPL28 in the oocytes [39]. They were identified also in the FF-EVs, so could be supplied by these particles to the oocyte and thereby influence oocyte development [39]. Taken together our current results and above mentioned data, VD alone or in co-treatment with I decreased the abundance of ribosomal proteins in the FF-EVs that could be a

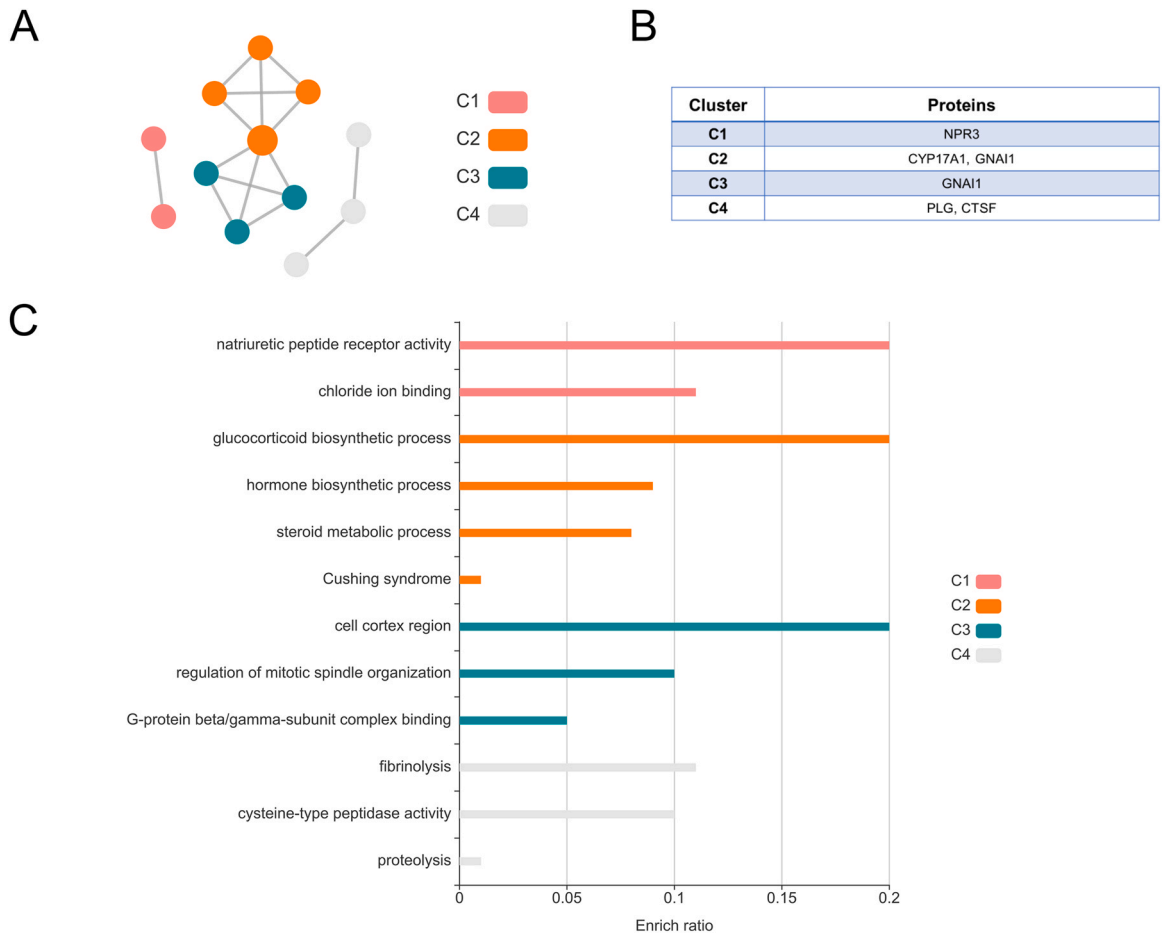

Fig. 9. Summary of functional annotation and pathway enrichment analysis of differentially abundant proteins (DAPs) evaluated in the VD *vs* VD+I group. (A) cirFunMap visualization of gene-list enrichment results into unique clusters. Each node represents an enriched term with color corresponding to the unique cluster according to term identity, while each edge represents a significant correlation between terms. (B) The table shows a list of proteins present in the corresponding clusters. (C) The bar chart represents the enriched terms found within each cluster (by color) and the bar length indicates the enrich ratio, calculated as "input gene number"/"background gene number". For each clusters, where numerous terms are enriched, only the top five with the highest enrich ratio are displayed. Detailed associations and annotations of all proteins to GO and KEGG pathway terms in this analysis are provided in Table S4.

possible novel mechanism of intrafollicular communication. However the exact functional role of ribosomal proteins enriched in the FF-EVs remains still unclear.

In the VD *vs* C comparison, we noted strong PPIs between two down-regulated proteins: protein disulfide-isomerase A3 (PDIA3) and A6 (PDIA6), annotated to "endoplasmic reticulum", "endoplasmic reticulum lumen", and "ribosome" GO terms. PDIA3 and PDIA6 regulate multiple protein functions, but predominantly participate in protein folding through the isomerization of protein disulphide bonds [45]. Our previous study demonstrated changes in the secondary protein structure after VD treatment in theca interna cells of the porcine ovarian follicle; namely an increased α-helical conformation was noted [24]. Therefore, the mechanism underlying the VD-induced changes in the secondary structure of proteins within porcine ovarian follicle might be associated with the alterations in the protein cargo of FF-EVs, including differentiated PDIA3 and PDIA6 abundance. It is worth noting that PDIA3 serves also as a VD receptor, which mediates its non-genomic action as reported in the ovary of pigs [27] and hens [46]. PDIA3-deficient carcinoma cell line A431 showed increased sensitivity to calcitriol [47]. Along this line, VD can modulate the response of the ovarian follicle to itself, modifying the content of PDIA3 receptor in the FF-EVs. The recent study by Chen et al. [48] demonstrated high expression of serum antibodies against PDIA3 in PCOS women with autoimmune thyroiditis. Thus, VD decreasing the abundance of PDIA3 in the FF-EVs might presumably reduce the production of anti-ovarian antibodies that can be useful for the PCOS diagnostic. To sum up, our current findings provide the evidence that VD modulates the FF-EVs protein cargo and the identified DAPs might indicate the potential pathways of its impact ovarian follicle functions under physiological and pathological conditions that requires further functional investigation.

The enrichment analysis of DAPs identified in the comparison I *vs* C revealed significant overrepresentation of GO terms such as "positive regulation of extrinsic apoptotic signaling pathway", "response to endoplasmic reticulum stress", "cell redox homeostasis", and "protein disulfide isomerase activity". They are represented by two down-regulated proteins: superoxide dismutase 2, mitochondrial (SOD2) and PDIA3, which are involved among others in oxidative stress; SOD2 is an antioxidant enzyme, while PDIA3 counters the aggregation of misfolded proteins that induce endoplasmic reticulum stress [49,50]. There is lack of research confirming that insulin directly induces oxidative stress. Nonetheless, conditions characterized by elevated insulin levels, such as hyperinsulinemia and insulin resistance, were associated with the increased oxidative stress [51]. In addition, the effect of I on the protein cargo of EVs *via* activation of PI3K/Akt signaling pathway was presented in colorectal cancer cells [52]. Knowing that oxidative stress causes the damage in the ovarian microenvironment that ultimately contribute to a decline in ovarian function [53], herein findings suggest that decreased enrichment of SOD2 and PDIA3 in the porcine FF-EVs might potentially attenuate their protective role in the ovarian oxidative stress. It should be highlighted that demonstrated SOD2 presence in the FF-EVs protein

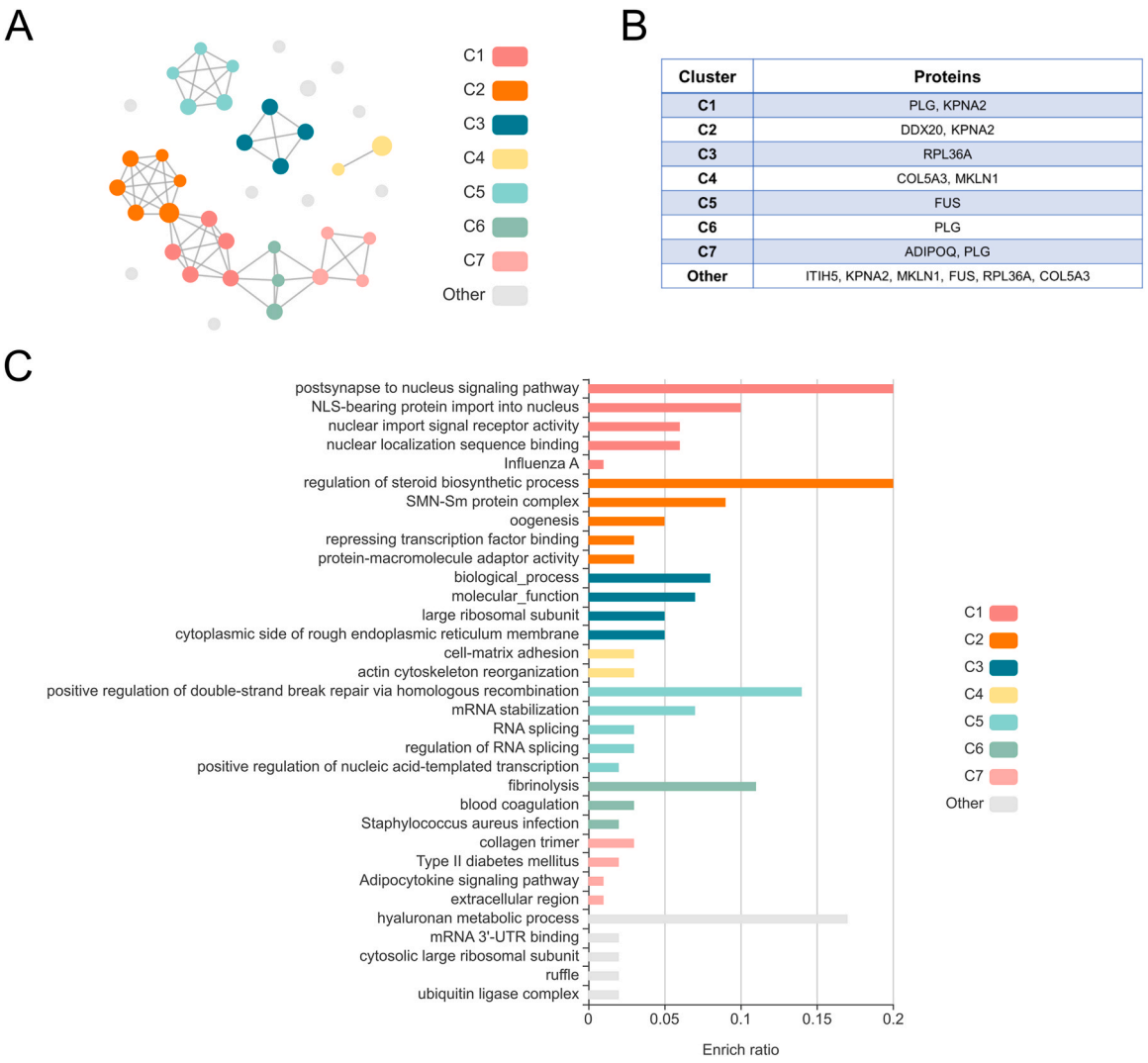

Cluster	Proteins
C1	PLG, KPNA2
C2	DDX20, KPNA2
C3	RPL36A
C4	COL5A3, MKLN1
C5	FUS
C6	PLG
C7	ADIPOQ, PLG
Other	ITIH5, KPNA2, MKLN1, FUS, RPL36A, COL5A3

Fig. 10. Summary of functional annotation and pathway enrichment analysis of differentially abundant proteins (DAPs) evaluated in the I *vs* VD+I group. (A) cirFunMap visualization of gene-list enrichment results into unique clusters. Each node represents an enriched term with color corresponding to the unique cluster according to term identity, while each edge represents a significant correlation between terms. (B) The table shows a list of proteins present in the corresponding clusters. (C) The bar chart represents the enriched terms found within each cluster (by color) and the bar length indicates the enrich ratio, calculated as "input gene number"/"background gene number". For each clusters, where numerous terms are enriched, only the top five with the highest enrich ratio are displayed. Detailed associations and annotations of all proteins to GO and KEGG pathway terms in this analysis are provided in Table S4.

cargo supports the hypothesis about the EV-mediated mitochondrial transfer [54] that is novel in the ovary and might improve the mitochondrial bioenergetics in recipient cells, including the oocyte.

Quantitative proteomic analysis revealed that the porcine FF-EVs are carriers of adiponectin (ADIPOQ), which was significantly differentiated in the comparisons VD+I *vs* C and VD+I *vs* I. ADIPOQ is the most abundant adipokine secreted by adipose tissue with the well-known insulin-sensitizing properties [55]. Apart from that many evidences suggested a direct role of ADIPOQ in reproductive tissues, including porcine ovarian follicle, where it induced ovarian steroidogenesis [56]. There is also a link between ADIPOQ and PCOS; ADIPOQ plasma and follicular fluid concentration was negatively correlated with insulin resistance in PCOS women [57]. Our previous study on rats with induced PCOS revealed similar effect of VD and I co-treatment on ADIPOQ protein; namely they increased its abundance in the rat uterus [58]. Collectively with another research, demonstrating peripheral insulin resistance in the uterus of PCOS-induced rats and its withdrawal after VD administration [59], the plausible ADIPOQ-mediated insulin-sensitizing effect following VD and I administration is proposed. Accordingly, Blandin et al. [60] showed that adipose tissue-derived EVs are stable ADIPOQ carriers and display insulin-sensitizing effects by binding to regular adiponectin receptors. Altogether, our current outcomes suggest that ADIPOQ enriched in the FF-EVs might ameliorate insulin resistance in the ovary, while its enhanced abundance in the VD+I group shed a new light on the EV-based therapeutic perspectives for ADIPOQ delivery during PCOS. However this hypothesis needs further confirmation.

5. Conclusions

The present research is the first to demonstrate the influence of VD and I on the porcine FF-EVs, including their characterization and proteomic cargo. The effect of VD and I on the FF-EVs concentration indicates that their interactions may impact EV release in the ovarian follicle. From the proteomic results, VD alone or in co-treatment with I affected mainly the abundance of ribosomal proteins, which could be a novel element of the intrafollicular communication. The I seems to be involved in the ovarian oxidative stress *via* down-regulation of SOD2 and PDIA3 proteins. Finally, ADIPOQ transferred by the FF-EVs could be a plausible protein marker of VD and I cross-talk, influencing insulin

sensitivity at the ovary level. To sum up, VD and I seem to be novel modulators of the porcine FF-EVs proteome and thereby could potentially modify ovarian follicle function *via* the EV-mediated pathway. However, the current proteomic results require further functional validation to precisely confirm their contribution to ovarian functions and strengthen the biological relevance.

CRediT authorship contribution statement

K.K.: Conceptualization, Investigation, Methodology, Visualization, Writing - Original Draft. B.Ś.: Investigation, Methodology. A.M.: Formal analysis. J.B.: Investigation. M.G.: Conceptualization, Formal analysis, Funding acquisition, Methodology, Project administration, Resources, Supervision, Writing - Original Draft, Writing - Review & Editing. All authors read and approved the final manuscript.

Ethical approval

The use of animals was in accordance with the Act of 15 of January 2015 on the Protection of Animals Used for Scientific or Educational Purposes and Directive 2010/63/EU of the European Parliament and the Council of 22 of September 2010 on the protection of animals used for scientific purposes.

Declaration of Competing Interest

The authors declare that they have no known competing financial interests or personal relationships that could have appeared to influence the work reported in this paper. No potential conflict of interests relevant to this article were reported.

Acknowledgments

Funding for this study was provided by the National Science Center, Poland (PRELUDIUM BIS 1 project no. 2019/35/O/NZ9/02678 to MG). The authors would like to thank the Department of Cell Biology and Imaging of the Institute of Zoology and Biomedical Research, the Jagiellonian University for the access to the transmission electron microscope (JEOL JEM 2100HT).

Appendix A. Supporting information

Supplementary data associated with this article can be found in the online version at doi:10.1016/j.repbio.2025.101040.

Data availability

The mass spectrometry proteomics data have been deposited to the ProteomeXchange Consortium via the PRIDE [61] partner repository with the dataset identifier PXD054450 and 10.6019/PXD054450.

References

[1] Monget P, McNatty K, Monniaux D. The crazy ovary. Genes 2021;12(6):928. https://doi.org/10.3390/genes12060928.
[2] Mikhael S, Punjala-Patel A, Gavrilova-Jordan L. Hypothalamic-pituitary-ovarian axis disorders impacting female fertility. Biomedicines 2019;7(1):5. https://doi.org/10.3390/biomedicines7010005.
[3] Sugiura K, Maruyama N, Akimoto Y, Matsushita K, Endo T. Paracrine regulation of granulosa cell development in the antral follicles in mammals. Reprod Med Biol 2023;22(1):e12538. https://doi.org/10.1002/rmb2.12538.
[4] Tesfaye D, Hailay T, Salilew-Wondim D, Hoelker M, Bitseha S, Gebremedhn S. Extracellular vesicle mediated molecular signaling in ovarian follicle: implication for oocyte developmental competence. Theriogenology 2020;150:70–4. https://doi.org/10.1016/j.theriogenology.2020.01.075.
[5] Jeppesen DK, Zhang Q, Franklin JL, Coffey RJ. Extracellular vesicles and nanoparticles: emerging complexities. Trends Cell Biol 2023;33(8):667–81. https://doi.org/10.1016/j.tcb.2023.01.002.
[6] Théry C, Zitvogel L, Amigorena S. Exosomes: composition, biogenesis and function. Nat Rev Immunol 2002;2(8):569–79. https://doi.org/10.1038/nri855.
[7] Santonocito M, Vento M, Guglielmino MR, Battaglia R, Wahlgren J, Ragusa M, et al. Molecular characterization of exosomes and their microRNA cargo in human follicular fluid: bioinformatic analysis reveals that exosomal microRNAs control pathways involved in follicular maturation. Fertil Steril 2014;102(6):1751–61. https://doi.org/10.1016/j.fertnstert.2014.08.005.
[8] Da Silveira JC, Veeramachaneni DN, Winger QA, Carnevale EM, Bouma GJ. Cell-secreted vesicles in equine ovarian follicular fluid contain miRNAs and proteins: a possible new form of cell communication within the ovarian follicle. Biol Reprod 2012;86(3):71. https://doi.org/10.1095/biolreprod.111.093252.
[9] Navakanitworakul R, Hung WT, Gunewardena S, Davis JS, Chotigeat W, Christenson LK. Characterization and small RNA content of extracellular vesicles in follicular fluid of developing bovine antral follicles. Sci Rep 2016;6:25486. https://doi.org/10.1038/srep25486.
[10] Grzesiak M, Popiolek K, Knapczyk-Stwora K. Extracellular vesicles in follicular fluid of sexually mature gilts' ovarian antral follicles - identification and proteomic analysis. 10.26402/jpp.2020.1.13 J Physiol Pharm 2020;71(1). https://doi.org/10.26402/jpp.2020.1.13.
[11] Muñoz EL, Fuentes FB, Felmer RN, Yeste M, Arias ME. Extracellular vesicles in mammalian reproduction: a review. Zygote 2022;30(4):440–63. https://doi.org/10.1017/S0967199422000090.
[12] Duval C, Wyse BA, Tsang BK, Librach CL. Extracellular vesicles and their content in the context of polycystic ovarian syndrome and endometriosis: a review. J Ovarian Res 2024;17(1):160. https://doi.org/10.1186/s13048-024-01480-7.
[13] Martinez RM, Baccarelli AA, Liang L, Dioni L, Mansur A, Adir M, et al. Body mass index in relation to extracellular vesicle-linked microRNAs in human follicular fluid. e3 Fertil Steril 2019;112(2):387–96. https://doi.org/10.1016/j.fertnstert.2019.04.001.
[14] Saeed-Zidane M, Linden L, Salilew-Wondim D, Held E, Neuhoff C, Tholen E, et al. Cellular and exosome mediated molecular defense mechanism in bovine granulosa cells exposed to oxidative stress. PLoS One 2017;12(11):e0187569. https://doi.org/10.1371/journal.pone.0187569.
[15] Wang L, Liu KF, Zhang XM. High throughput circRNAs sequencing profile of follicle fluid exosomes of polycystic ovary syndrome patients. J Cell Physiol 2019;234(9):15537–47. https://doi.org/10.1002/jcp.28201.
[16] Yang Y, Lang P, Zhang X, Wu X, Cao S, Zhao C, et al. Molecular characterization of extracellular vesicles derived from follicular fluid of women with and without PCOS: integrating analysis of differential miRNAs and proteins reveals vital molecules involving in PCOS. J Assist Reprod Genet 2023;40(3):537–52. https://doi.org/10.1007/s10815-023-02724-z.
[17] Li M, Hu S, Sun J, Zhang Y. The role of vitamin D3 in follicle development. J Ovarian Res 2024;17(1):148. https://doi.org/10.1186/s13048-024-01454-9.
[18] Grzesiak M, Tchurzyk M, Socha M, Sechman A, Hrabia A. An overview of the current known and unknown roles of vitamin D3 in the female reproductive system: lessons from farm animals, birds, and fish. Int J Mol Sci 2022;23(22):14137. https://doi.org/10.3390/ijms232214137.
[19] Kamińska K, Grzesiak M. The relationship between vitamin D3 and insulin in polycystic ovary syndrome - a critical review. 10.26402/jpp.2021.1.02 J Physiol Pharm 2021;72(1). https://doi.org/10.26402/jpp.2021.1.02.
[20] Maestro B, Davila N, Carranza MC, Calle C. Identification of a vitamin D response element in the human insulin receptor gene promoter. J Steroid Biochem Mol Biol 2003;84(2-3):223–30. https://doi.org/10.1016/s0960-0760(03)00032-3.
[21] Kamińska K, Świderska B, Malinowska A, Grzesiak M. Tandem mass tag-based proteomic analysis of granulosa and theca interna cells of the porcine ovarian follicle following in vitro treatment with vitamin D3 and insulin alone or in combination. J Proteom 2025;310:105318. https://doi.org/10.1016/j.jprot.2024.105318.
[22] Grzesiak M, Herian M, Kamińska K, Ajersch P. Insight into vitamin D3 action within the ovary-Basic and clinical aspects. Adv Protein Chem Struct Biol 2024;142:99–130. https://doi.org/10.1016/bs.apcsb.2024.04.003.
[23] Akins EL, Morrissette MC. Gross ovarian changes during estrus cycle of swine. Am J Vet Res 1968;29(10):1953–7.
[24] Kamińska K, Wiercigroch E, Małek K, Grzesiak M. Biomolecular composition of porcine ovarian follicles following in vitro treatment of vitamin D3 and insulin alone or in combination. Reprod Biol 2023;23(4):100818. https://doi.org/10.1016/j.repbio.2023.100818.
[25] Rice S, Pellatt LJ, Bryan SJ, Whitehead SA, Mason HD. Action of metformin on the insulin-signaling pathway and on glucose transport in human granulosa cells. J Clin Endocrinol Metab 2011;96(3):E427–35. https://doi.org/10.1210/jc.2010-2060.
[26] Smolikova K, Mlynarcikova A, Scsukova S. Effect of 1α,25-dihydroxyvitamin D3 on progesterone secretion by porcine ovarian granulosa cells. Endocr Regul 2013;47(3):123–31. https://doi.org/10.4149/endo_2013_03_123.
[27] Grzesiak M, Knapczyk-Stwora K, Slomczynska M. Vitamin D3 in ovarian antral follicles of mature gilts: expression of its receptors and metabolic enzymes, concentration in follicular fluid and effect on steroid secretion in vitro. Theriogenology 2021;160:151–60. https://doi.org/10.1016/j.theriogenology.2020.11.006.
[28] Reshi QUA, Hasan MM, Dissanayake K, Fazeli A. Isolation of extracellular vesicles (EVs) using benchtop size exclusion chromatography (SEC) columns. Methods Mol Biol 2021;2273:201–6. https://doi.org/10.1007/978-1-0716-1246-0_14.
[29] Kamińska K, Godakumara K, Świderska B, Malinowska A, Midekessa G, Sofińska K, et al. Characteristics of size-exclusion chromatography enriched porcine follicular fluid extracellular vesicles. Theriogenology 2023;205:79–86. https://doi.org/10.1016/j.theriogenology.2023.04.010.
[30] Gabryś J, Kij-Mitka B, Sawicki S, Kochan J, Nowak A, Łojko J, et al. Extracellular vesicles from follicular fluid may improve the nuclear maturation rate of *in vitro*

matured mare oocytes. Theriogenology 2022;188:116–24. https://doi.org/10.1016/j.theriogenology.2022.05.022.
[31] Tyanova S, Temu T, Cox J. The MaxQuant computational platform for mass spectrometry-based shotgun proteomics. Nat Protoc 2016;11(12):2301–19. https://doi.org/10.1038/nprot.2016.136.
[32] Bu D, Luo H, Huo P, Wang Z, Zhang S, He Z, et al. KOBAS-i: intelligent prioritization and exploratory visualization of biological functions for gene enrichment analysis. Nucleic Acids Res 2021;49(W1):W317–25. https://doi.org/10.1093/nar/gkab447.
[33] Szklarczyk D, Kirsch R, Koutrouli M, Nastou K, Mehryary F, Hachilif R, et al. The STRING database in 2023: protein-protein association networks and functional enrichment analyses for any sequenced genome of interest. Nucleic Acids Res 2023;51(D1):D638–46. https://doi.org/10.1093/nar/gkac1000.
[34] Payet T, Valmori M, Astier J, Svilar L, Sicard F, Tardivel C, et al. Vitamin D modulates lipid composition of adipocyte-derived extracellular vesicles under inflammatory conditions. Mol Nutr Food Res 2023;67(22):e2300374. https://doi.org/10.1002/mnfr.202300374.
[35] Lino M, Garcia-Martin R, Muñoz VR, Ruiz GP, Nawaz A, Brandão BB, et al. Multi-step regulation of microRNA expression and secretion into small extracellular vesicles by insulin. Cell Rep 2024;43(7):114491. https://doi.org/10.1016/j.celrep.2024.114491.
[36] Ostrowski M, Carmo NB, Krumeich S, Fanget I, Raposo G, Savina A, et al. Rab27a and Rab27b control different steps of the exosome secretion pathway. sup pp 1-13 Nat Cell Biol 2010;12(1):19–30. https://doi.org/10.1038/ncb2000.
[37] Payet T, Astier J, Bournot L, Sicard F, Robert S, Lacroix R, et al. Vitamin D modulates the content of inflammatory microRNAs in extracellular vesicles from human adipocyte cells in inflammatory context. Biofactors 2025;51(1):e70003. https://doi.org/10.1002/biof.70003.
[38] Zhou X, Liao WJ, Liao JM, Liao P, Lu H. Ribosomal proteins: functions beyond the ribosome. J Mol Cell Biol 2015;7(2):92–104. https://doi.org/10.1093/jmcb/mjv014.
[39] Uzbekova S, Almiñana C, Labas V, Teixeira-Gomes AP, Combes-Soia L, Tsikis G, et al. Protein cargo of extracellular vesicles from bovine follicular fluid and analysis of their origin from different ovarian cells. Front Vet Sci 2020;7:584948. https://doi.org/10.3389/fvets.2020.584948.
[40] da Silveira JC, Andrade GM, Del Collado M, Sampaio RV, Sangalli JR, Silva LA, et al. Supplementation with small-extracellular vesicles from ovarian follicular fluid during in vitro production modulates bovine embryo development. PLoS One 2017;12(6):e0179451. https://doi.org/10.1371/journal.pone.0179451.
[41] Matsuno Y, Kanke T, Maruyama N, Fujii W, Naito K, Sugiura K. Characterization of mRNA profiles of the exosome-like vesicles in porcine follicular fluid. PLoS One 2019;14(6):e0217760. https://doi.org/10.1371/journal.pone.0217760.
[42] Ochkasova A, Arbuzov G, Malygin A, Graifer D. Two "edges" in our knowledge on the functions of ribosomal proteins: the revealed contributions of their regions to translation mechanisms and the issues of their extracellular transport by exosomes. Int J Mol Sci 2023;24(14):11458. https://doi.org/10.3390/ijms241411458.
[43] Chen GH, Ren JG, Xia HF, Zhang HJ, Wang KM, Zhang LZ, et al. Ribosomal protein L36-mediated selective loading of microRNA-4432 into extracellular vesicles contributes to perivascular cell dysfunction in venous malformations. Br J Dermatol 2025;192(4):717–27. https://doi.org/10.1093/bjd/ljae492.
[44] Thankam FG, Huynh J, Fang W, Chen Y, Agrawal DK. Exosomal-ribosomal proteins-driven heterogeneity of epicardial adipose tissue derived stem cells under ischemia for cardiac regeneration. J Tissue Eng Regen Med 2022;16(4):396–408. https://doi.org/10.1002/term.3289.
[45] Appenzeller-Herzog C, Ellgaard L. The human PDI family: versatility packed into a single fold. Biochim Biophys Acta 2008;1783(4):535–48. https://doi.org/10.1016/j.bbamcr.2007.11.010.
[46] Hrabia A, Kamińska K, Socha M, Grzesiak M. Vitamin D3 receptors and metabolic enzymes in hen reproductive tissues. Int J Mol Sci 2023;24(23):17074. https://doi.org/10.3390/ijms242317074.
[47] Nowak JI, Olszewska AM, Piotrowska A, Myszczyński K, Domżalski P, Żmijewski MA. PDIA3 modulates genomic response to 1,25-dihydroxyvitamin D3 in squamous cell carcinoma of the skin. Steroids 2023;199:109288. https://doi.org/10.1016/j.steroids.2023.109288.
[48] Chen Z, Zhang C, Meng C, Hu Y, Niu Y, Gao B, et al. Unveiling the link: anti-protein disulfide isomerase A3 autoantibody expression and polycystic ovary syndrome risk in euthyroid autoimmune thyroiditis women. J Ovarian Res 2024;17(1):247. https://doi.org/10.1186/s13048-024-01569-z.
[49] Mahmood F, Xu R, Awan MUN, Song Y, Han Q, Xia X, et al. PDIA3: Structure, functions and its potential role in viral infections. Biomed Pharm 2021;143:112110. https://doi.org/10.1016/j.biopha.2021.112110.
[50] Jomova K, Alomar SY, Alwasel SH, Nepovimova E, Kuca K, Valko M. Several lines of antioxidant defense against oxidative stress: antioxidant enzymes, nanomaterials with multiple enzyme-mimicking activities, and low-molecular-weight antioxidants. Arch Toxicol 2024;98(5):1323–67. https://doi.org/10.1007/s00204-024-03696-4.
[51] Tangvarasittichai S. Oxidative stress, insulin resistance, dyslipidemia and type 2 diabetes mellitus. World J Diabetes 2015;6(3):456–80. https://doi.org/10.4239/wjd.v6.i3.456.
[52] Liem M, Ang CS, Mathivanan S. Insulin mediated activation of PI3K/Akt signalling pathway modifies the proteomic cargo of extracellular vesicles. 10.1002/pmic.201600371 Proteomics 2017;17(23-24). https://doi.org/10.1002/pmic.201600371.
[53] Ammar OF, Massarotti C, Mincheva M, Sharma K, Liperis G, Herraiz S, et al. Oxidative stress and ovarian aging: from cellular mechanisms to diagnostics and treatment. Hum Reprod 2024;39(7):1582–6. https://doi.org/10.1093/humrep/deae082.
[54] Dozio V, Sanchez JC. Characterisation of extracellular vesicle-subsets derived from brain endothelial cells and analysis of their protein cargo modulation after TNF exposure. J Extra Vesicles 2017;6(1):1302705. https://doi.org/10.1080/20013078.2017.1302705.
[55] Balistreri CR, Caruso C, Candore G. The role of adipose tissue and adipokines in obesity-related inflammatory diseases. Mediat Inflamm 2010;2010:802078. https://doi.org/10.1155/2010/802078.
[56] Maleszka A, Smolinska N, Nitkiewicz A, Kiezun M, Chojnowska K, Dobrzyn K, et al. Adiponectin expression in the porcine ovary during the oestrous cycle and its effect on ovarian steroidogenesis. Int J Endocrinol 2014;2014:957076. https://doi.org/10.1155/2014/957076.
[57] Lin K, Sun X, Wang X, Wang H, Chen X. Circulating adipokine levels in nonobese women with polycystic ovary syndrome and in nonobese control women: a systematic review and meta-analysis. Front Endocrinol 2021;11:537809. https://doi.org/10.3389/fendo.2020.537809.
[58] Pich K, Rajewska J, Kamińska K, Tchurzyk M, Szlaga A, Sambak P, et al. Effect of vitamin D3 on chemerin and adiponectin levels in uterus of polycystic ovary syndrome rats. Cells 2023;12(16):2026. https://doi.org/10.3390/cells12162026.
[59] Kamińska K, Tchurzyk M, Fraczek O, Szlaga A, Sambak P, Tott S, et al. Effect of vitamin D3 on uterine morphology and insulin signaling in a polycystic ovary syndrome (PCOS) rat model. Ann Anim Sci 2024;24(4):1197–209. https://doi.org/10.2478/aoas-2024-0038.
[60] Blandin A, Amosse J, Froger J, Hilairet G, Durcin M, Fizanne L, et al. Extracellular vesicles are carriers of adiponectin with insulin-sensitizing and anti-infla mmatory properties. Cell Rep 2023;42(8):112866. https://doi.org/10.1016/j.celrep.2023.112866.
[61] Perez-Riverol Y, Bai J, Bandla C, et al. The PRIDE database resources in 2022: a hub for mass spectrometry-based proteomics evidences. Nucleic Acids Res 2022;50:D543–52. https://doi.org/10.1093/nar/gkab1038.